The Thesis Committee for Xin Liu
Certifies that this is the approved version for the following thesis:

Feasibility of Prediction of Principal stress from reflection seismic data

APPROVED BY

SUPERVISING COMMITTEE

Supervisor:

Mrinal K. Sen

Peter B. Flemings

Kyle T. Spikes

Feasibility of Prediction of Principal Stress from Reflection Seismic Data

by

Xin Liu, B.S. Geological Sciences

Thesis

Presented to the Faculty of the Graduate School of

The University of Texas at Austin

in Partial Fulfillment

of the Requirements

for the Degree of

Master of Science in Geological Sciences

The University of Texas at Austin

December 2021

Dedication

I would like to thank and dedicate this work to my friends, family, and all the people who helped me get here today and get through this pandemic. I would like to thank my girlfriend who supports me from the other side of the world.

Acknowledgments

The author wishes to acknowledge and thank the UT Geofluids consortium for supporting my research. And I would like to acknowledge Maria Nikolinakou and Deniz Ranjpour for providing me with the stress model and the laboratory measurements.

Abstract

Feasibility of Prediction of Principal Stress from Reflection Seismic Data

Xin Liu, M.S. Geo. Sci.

The University of Texas at Austin, 2021

Supervisor: Mrinal K. Sen

Orientations and magnitudes of subsurface principal stresses are crucial information for understanding the structure and tectonic processes inside the Earth. This knowledge is not only important in geotechnical applications but also vital in the petroleum industry. For example, the stress state in the Earth's crust controls stress concentration around wellbores and, therefore, plays a critical role in wellbore instability and fluid flow in fractured reservoirs.

Several efforts to obtain subsurface principal stresses have been reported in published articles. However, most of these studies are based on the analyses of well log data and core plug measurements, which only provide accurate information at some specific locations. On the other hand, seismic inversion is one popular approach that aims at predicting some of the physical properties from observed seismic data indirectly. It can provide an even greater comprehensive description of the subsurface geology but at a lower vertical resolution.

Using laboratory data and theoretical modeling, several researchers have reported that subsurface stress can lead to seismic anisotropy. Noticeable anomalies in field seismic data due to anisotropy, such as non-hyperbolic move-out, AVO, and anomalous waveforms have also been

reported in the literature. However, no field scale estimation of subsurface stress variation from seismic data has yet been carried out. Therefore, in my research, I attempt to examine the feasibility of predicting principal stresses from seismic inversion based on a stress-anisotropy relationship.

Forward modeling is the foundation of seismic inversion. The finite-difference (FD) method is the most widely used forward modeling method in seismic waveform inversion. However, it suffers from the stair-casing problem, which introduces unwanted noise from irregular model parameter boundaries. Therefore, I develop an improved mesh-free method to accurately describe the irregular boundaries.

My work entails the following three closely related steps:

1) Relate stress to anisotropy

Rock physics can be used to create models for subsurface lithologies, which describe the petrophysical and elastic behavior through a set of empirical, heuristic, and theoretical relations. In my current work, I derive stress to stiffness relationship from laboratory measurements from a mudrock sample. This analysis demonstrates that the stiffnesses are anisotropic under vertical stress.

2) Mesh-free anisotropy media forward modeling

I develop the radial basis-function generated finite-difference (RBF-FB) method for the mesh-free discretization scheme. Then I generalize this forward modeling method for anisotropic media and test it on some synthetic models. I employ this method to generate synthetic seismograms based on a realistic model derived from laboratory data and demonstrate the effect of stress on seismic data.

3) Seismic inversion sensitivity analysis

I generate synthetic seismograms for simple models for which stiffnesses are computed for different stress magnitudes and directions. These data are then inverted by a global optimization method called Very Fast Simulated Annealing (VFSA) to demonstrate the feasibility of seismic inversion for principal stress. The forward modeling procedure in the VFSA method is carried out via the mesh-free RBF-FD method. My initial work shows that the magnitudes and angles of the stress have noticeable effects on the seismic response that can be estimated by seismic inversion.

Thesis Table of Contents Draft

List of Tables

Chapter 1: Introduction

1.1 Motivation

The processes that contribute to the in-situ stress state primarily include plate tectonic driving forces, gravitational loading, and some human activities such as hydraulic fracturing and drilling. Plate driving forces cause the motions of the lithospheric plates that form the crust of the Earth. Gravitational loading forces include topographic loads and loads owing to lateral density contrasts and lithospheric buoyancy. These are modified by the local processes such as volcanism, earthquakes (fault slip), and salt diapirism. Especially, the presence of salt significantly perturbs the stress distribution (Nikolinakou *et al*., 2012). On the other hand, human activities such as mining and fluid extraction or injection can also cause local stress changes.

A comprehensive understanding of subsurface stress distribution is vital for understanding the Earth's interior structures and tectonic movement history. Moreover, in the oil industry, significant oil reserves exist against and beneath the salt. Salt structures control the initiation, maturation, and trapping of hydrocarbons (e.g., Luo *et al.*, 2012; Nikolinakou *et al.*, 2012; Heidari *et al*., 2017; McBride *et al.*, 1998). Understanding the stress and pore pressure near the salt is essential for the development of a geomechanical model that can guide well design as part of an integrated process to minimize cost and maximize safety.

Widespread studies have been conducted and different measurement methods and theories or empirical relationships have been established for estimating the stress state in the Earth's crust. The underground stress state can be described by three mutually orthogonal principal stress components. Most studies have been based on well logs and core plug measurements, which only provide accurate information at some specific locations (e.g., Fang *et al*., 2012, 2013; Ong *et al*., 2016).

Seismic anisotropy has been increasingly used as a tool to investigate the Earth's interior stress distribution. Differential principal stress in the subsurface can create anisotropy through some mechanisms such as the closure of aligned cracks and mechanical discontinuities present in the rock mass (e.g., Tromp *et al*., 2019; Verdon *et al*., 2008; Sayers and Dasgupta, 2019). Anisotropy provides a convenient way to monitor stress orientations in the crust, especially when there is a lack of geodetic observations (well logging, interferometric synthetic aperture radar, etc.). Thus, understanding how seismic anisotropy is affected by stress is important for predicting principal stresses from seismic data.

Many approaches have been proposed to calculate the effect of stress-induced anisotropy on the seismic data (e.g., Gurevich *et al*., 2010; Fichtner *et al*., 2013; Collet *et al*., 2012). The effect of stress on the accuracy of seismic inversion has also been investigated (e.g., Tromp *et al*., 2018). However, there are different causes of seismic anisotropy, including intrinsic anisotropy, layer- or fracture-induced anisotropy, and stress-induced anisotropy (Sarkar *et al*., 2003). Therefore, it is important to distinguish the contribution of the stress-induced anisotropy from total anisotropy (e.g., Wang *et al*., 2013; Wang *et al*., 2015; David *et al*., 2018; Asaka *et al*., 2016). On the other hand, by measuring the physical properties of rock samples under different stress, it is possible to explicitly extract the relationship between stress and anisotropy. In my research, I focus primarily on stress-induced anisotropy and its effects on seismic data to estimate anisotropy/stress parameters.

1.2 Objectives

The ultimate goal of my research is to establish a robust and practical method to predict principal stresses from seismic data. In this work, I examine the feasibility of predicting the subsurface stress state from seismic data. To achieve this goal, I implement three processes to bridge the gap between seismic data and subsurface principal stress.

The first step is to establish a relationship between stress and stiffness based on the physical properties of rock samples measured under different stress and stiffness. I assume that the subsurface media are tilted transversely isotropic (TTI). This may not be true in general but is quite close to the case of layered sedimentary rocks considered here. A transversely isotropic medium with a vertical symmetry axis (VTI) is a special case of TTI media. Here I illustrate my method based on VTI media. Laboratory measurements (Ranjpour, 2020) under each stress contain P- and S-wave velocities measured at vertical and horizontal directions, respectively, the P-wave velocity at an inclined angle, and the sample density. Based on these measurements, I will calculate the corresponding anisotropy under different stress. Note that the calculated stiffnesses are confined by the strain energy constraints, therefore, I employ the maximum likelihood method to obtain the most feasible stress-stiffness relationship.

In seismic inversion workflows, forward modeling is the fundamental part and consumes most of the computation. However, the conventional finite-difference (FD)method utilizes regular grids to discretize model parameters, which leads to an inaccurate description of irregular model boundaries. This problem is called the stair-casing problem. On the other hand, stress variations around interfaces are crucial for drilling analysis that should not be confused with numerical modeling artifacts. To alleviate this problem, I use mesh-free discretization, which has been proved to be effective in dealing with the stair-casing problem and the overs-sampling problem (Fornberg and Flyer 2015). In this work, I implement acoustic TTI media seismic forward modeling with the mesh-free RBF-FD method.

In the final step, based on the stress-stiffness relationship obtained from lab measurements analysis, it is crucial to determine if seismic data are sensitive to subsurface stress. And if so, are they sensitive enough for predicting subsurface stress? Among the numerous inversion methods, the very fast simulated annealing (VFSA) is a global search method invented to avoid local minima (e.g., Sen and Stoffa, 1995; Datta *et al*., 2018). Therefore, I employ the VFSA to examine the sensitivity of seismic data to subsurface stress. Note that, the mesh-free RBF-FD method is used in the VFSA as the forward operator. The final results on some simple models demonstrate the feasibility of predicting subsurface stress from seismic data.

1.3 Thesis organization

This thesis has 5 chapters. Chapter 1 outlines the motivation for conducting this work, the overall objectives of this research, and the organization/outline presented within this thesis. Chapter 2 introduces seismic anisotropy and derives the stress-stiffness relationship through rock physics analysis of lab measurements. Chapter 3 illustrates the mesh-free RBF-FD method for seismic forward modeling and applies it to acoustic TI media modeling. Chapter 4 demonstrates the feasibility of inverting subsurface stress from seismic data via applying VFSA on some simple models. Chapter 5 concludes the thesis with a detailed summary of the outcomes achieved from the researches in Chapters 2, 3, and 4.

Chapter 2: Rock physics analysis

In this thesis, I am focused on the two-dimensional (2D) stress state. In situ subsurface stress could be characterized by principal stresses, which represent the maximum and minimum normal stresses on a plane (when rotated through an angle) on which there is no shear stress. Under this condition, the maximum normal stress is referred to as the maximum principal stress. The magnitude and angle of the maximum principal stress could be the major factor that affects the rock physics properties, such as stiffness and density, therefore influencing the seismic response of the subsurface media.

The lab measurements of one rock sample under different axial effective stress demonstrate an anisotropic behavior. Therefore, based on the TTI anisotropy theory, I derive the most likely stress-stiffness relationship from the lab measurements.

2.1 Seismic anisotropy

Anisotropy is the variation of a physical property depending on the direction in which it is measured; it is different from heterogeneity, which is the lack of spatial uniformity, the opposite of homogeneity. However, even though anisotropy and heterogeneity describe different phenomena, they are related because anisotropy arises from ordered heterogeneity that is smaller than the seismic wavelength λ_W , and every heterogeneous material is anisotropic to a degree at some scale λ_s .

Anisotropy can be produced by multiple physical processes at different spatial scales. It exists from the microscale (crystal scale) to the macroscale, where it can be observed by seismic waves that have wavelengths up to hundreds of kilometers. Therefore, anisotropy may be strongly dependent on wavelength λ_W , as it results from the average properties of aligned or partially aligned heterogeneity, as shown in Figure 1.1.

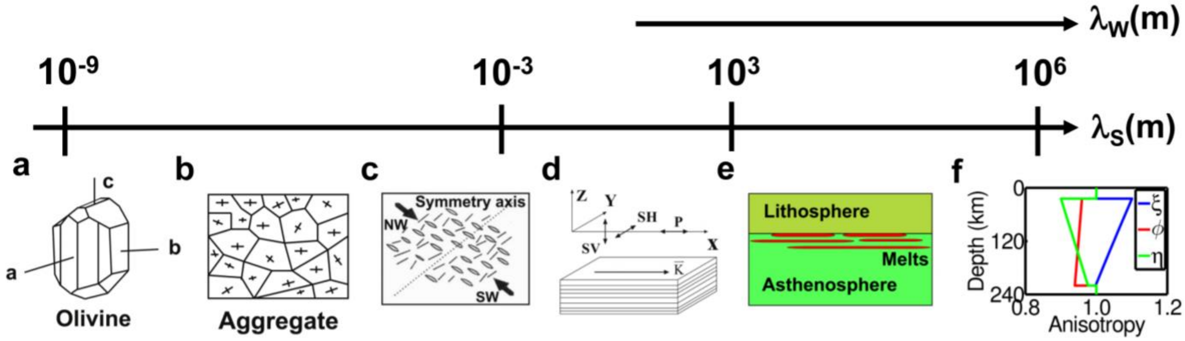

Figure 2.1: The existence of anisotropy from the microscale to the macroscale: (a) The anisotropic olivine crystal. (b) The anisotropic aggregate is an example of re-crystallographic preferred orientation. (c) Cracks filled with fluid inclusions with a symmetry axis. (d) A finely layered transversely isotropic model with a vertical symmetry. (e) Seismic anisotropy at the lithosphere and asthenosphere boundary. (f) Radial anisotropy parameters in the upper mantle (Wang *et al.*, 2013).

Based on different mechanisms, seismic anisotropy is classified into three categories:

Intrinsic Anisotropy: A solid has intrinsic anisotropy when it is homogeneously anisotropic down to the smallest particle size, which may be caused by lattice or crystallographic preferred orientation. This kind of anisotropy usually demonstrates a strong effect for short-wavelength laboratory measurements, but it can also be observed when the preferred orientation has a scale of seismic wavelength, and otherwise, it will be hard to observe on long-wavelength seismic reflection data as the short-wavelength anisotropic effect is filtered, which is referred to as the upscaling process (e.g., Schoenberg and Muir, 1989; Wang *et al.*, 2015).

Layer- or fracture-induced Anisotropy: The presence of aligned cracks and fine layering is an important mechanism of seismic anisotropy (Schoenberg and Sayers, 1995). It is well known that the small-scale, or microstructural, factors include (Bandyopadhyay, 2009): (1) variations in the spatial distribution of grains and minerals; (2) grain morphology and (3) aligned fractures, cracks and pores, and the nature of their infilling material (e.g. clays, hydrocarbons, water, etc.).

During the deposition process, anisotropy is caused by the periodic layering associated with changes in sediment type, which produces materials of different grain sizes, and also by the directionality of the transporting medium which tends to order the grains under gravity by grain sorting. Fracturing and some diagenetic processes such as compaction and dewatering of clays, and alteration, etc. are post-depositional processes that can cause anisotropy (Maultzsch *et al.*, 2003).

Stress-induced Anisotropy: Stress has the potential to affect most petrophysical rock properties. Schwartz *et al.* (1994) demonstrated two very different rock models, namely a cracked model and a weakly consolidated granular model, for stress-induced anisotropy. For the cracked model, stress-induced anisotropy is caused by the opening or closing of the compliant and crack-like parts of the pore space due to tectonic stresses. For the weakly consolidated granular model (e.g., Oda *et al.*, 1985; Arthur *et al.*, 1977; Ouadfel and Rothenbug, 1999), stress-induced anisotropy is illustrated as the realignment of microscale particles, which is referred to as fabric (Kuhn *et al.*, 2015) or platy grains (Bandyopadhyay, 2009). The cracked model suggests a greater velocity change in the direction perpendicular to the stress direction due to the closure of "soft cracks" normal to the direction of applied stress (Sayers *et al.*, 2002). While the weakly consolidated granular model suggests the greater velocity change is parallel to the loading direction of stress because the fabric or platy grains are re-aligned perpendicular to the direction of applied stress (Adams *et al.*, 2013). Here in this thesis, I derive the stress-stiffness relationship based on the rock physics analysis of measured seismic parameters under different vertical stresses.

Of the three causes for seismic anisotropy, stress-induced is the most interesting one due to its potential to predict in situ principal stresses (e.g., Rasolofosaon, 1998; Crampin *et al.*, 1984). However, it is a challenge to distinguish the stress-induced anisotropy from the intrinsic anisotropy and the layer- or fracture-induced anisotropy. Some claimed that most conventional unfractured reservoir rocks, such as sands, sandstones, and carbonates, show very little intrinsic anisotropy in an unstressed state (Bandyopadhyay, 2009). However, in the presence of shale, clay, and fine periodic layers, the seismic response shows similar anisotropic behavior as the stress-induced anisotropy (Zheng *et al.*, 2009). The magnitudes of different seismic anisotropy remain to be investigated. A priori information and geological knowledge can be used to determine possible causes of anisotropy.

2.2 Rock physics modeling

It is possible to establish a relationship between stress and stiffness based on the physical properties of rock samples measured under different stress and stiffness (Spikes, 2014). To build the rock physics model, firstly, I assume that the subsurface media are transversely isotropic (TI), which may not be true in general but is quite close to the case of layered sedimentary rocks. A transversely isotropic medium with a vertical symmetry axis (VTI) is a special case of TI media. When VTI media is rotated, it is called tilted transversely isotropic (TTI) media, and the rotation angle is referred to as the tilt angle. In my work, I assume that the anisotropy is induced by stress. As shown in Figure 2.2 (a) (Adams *et al.*, 2013), platy clay grains have a range of orientations. In this case, it is assumed to be isotropic or very weakly anisotropic. However, under uniaxial strain conditions, porosity has decreased following uniaxial compaction and there are alignments of the platy clay grains parallel to the horizontal axis, as shown in Figure 2.2 (b) and mark by red boxes. Velocity in the re-alignment direction is greater than that is perpendicular to the re-alignment direction. Therefore, the rock becomes anisotropic with a symmetric axis parallel to the direction of applied stress, which means it is a TI media with the tilted angle parallel to the direction of applied stress.

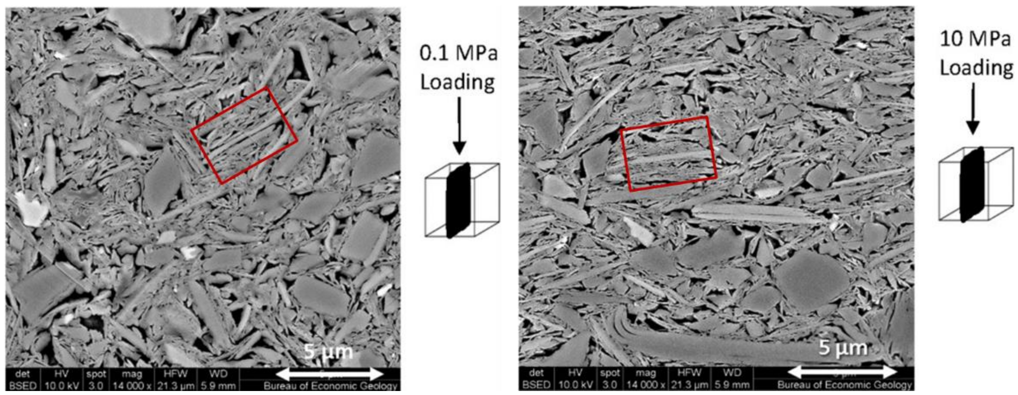

(a) (b)

Figure 2.2: Illustration of the stress-induced anisotropy. Back scattered electron microscopy (BSEM) images of Resedimented Boston Blue Clay loaded to different vertical effective stress (Adams *et al.*, 2013).

When considering anisotropy in the coordinates of the stress direction, the TI media is reduced to VTI media. Therefore, I will carry out my derivation based on VTI media theory.

There are plenty of researches about the rock physics behavior under variant stress (e.g., Abdulhadi, 2009). Among them, Ranjpour (2020) carried out laboratory measurements on a mudrock specimen from Eugene Island – Gulf of Mexico. Mudrocks are primarily composed of connected pores filled with fluid, platy clay minerals, and quasi-spherical silt grains (commonly quartz). In this experiment, the rock was loaded with different vertical effective stress under uniaxial strain. Rock physical properties were measured under 8 vertical stress from 2.8 MPa to 9.8 MPa. These measured properties include: 1) vertical and horizontal compressional wave velocities, 2) vertical and horizontal shear wave velocities, 3) vertical compressional wave velocity at an inclined angle; 4) and the sample density. Those properties are displayed in Figure 2.3, where V_{pH} is the horizontal compressional wave velocity, $V_{p\Phi}$ is the inclined compressional wave velocity, V_{pV} is the vertical compressional wave velocity, V_{sHH} is the 90 degrees incident shear wave velocity, V_{sVV} is the 0-degree incident shear wave velocity. As shown in Figure 3.3, velocities vary under uniaxial strain with increasing vertical effective stress. The velocity changes of different directions demonstrate anisotropic behavior, which indicates the presence of stress-induced anisotropy. Moreover, the seismic velocity is stress-dependent and the anisotropy is increasing with stress. The lab measurements demonstrate a greater velocity in the direction of perpendicular to the stress direction, which could be explained by the platy grain re-alignment model described in Figure 2.2.

Unlike the theoretical tock physics models described in the previous paragraphs, I derive an empirical relation between anisotropy parameters and vertical stress, which is described below.

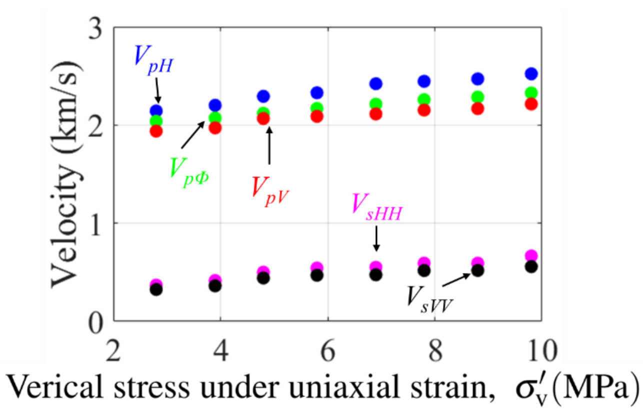

Figure 2.3: Mean velocity measurements as a function of vertical effective stress for uniaxial strain conditions (Ranjpour, 2020).

2.2.1 Group velocity to phase velocity transformation

There are at least two kinds of velocities to characterize seismic wave propagation in anisotropic media: group velocity and phase velocity (Helbig, 1994). The group velocity of a wave is the velocity with which the overall envelope shape of the wave's amplitudes, known as the modulation or envelope of the wave propagates through space. The phase velocity of a wave is the rate at which an individual plane wave or frequency propagates in any medium. This is the velocity at which the phase of any one frequency component of the wave travels. For such a component, any given phase of the wave (for example, the crest) will appear to travel with the phase velocity.

In a lossless isotropic medium, group velocity and phase velocity are identical. However, in anisotropic media, the two velocities are different. For VTI media, the illustration of the relationship between group and phase velocities is shown in Figure 2.4 (Tsvankin, 2001).

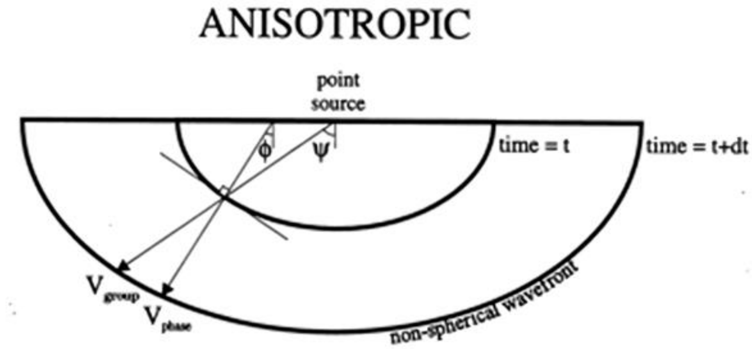

Figure 2.4: Illustration of the relationship between group and phase velocities in VTI media (from Tsvankin 2001.

The velocities measured in the laboratory such as those in Ranjpour's (2020) experiment are all group velocities. In general, stiffness is calculated by phase velocities rather than group velocities. Under the VTI media assumption, at propagation angle equals 0 degrees or 90 degrees, phase velocities and group velocities are identical. However, the group compressional wave velocity $V_{p\Phi}$ at inclined angle Φ should be transformed to phase velocity for stiffness calculation. Based on the VTI assumption, the group velocities are transformed to phase velocities by the following equation (Dellinger and Vernik, 1994):

$$\begin{cases} V_{phase} = \dfrac{V_{group}^2}{\sqrt{V_{group}^2 + \left(\dfrac{dV_{group}}{d\psi}\right)^2}} \\ \phi = \psi - \arctan\left(\dfrac{dV_{group} / d\psi}{V_{group}}\right) \end{cases}. \tag{2.1}$$

Note that in Equation (2.1), V_{phase} and V_{group} are the phase and group velocities of the VTI media, respectively. ϕ and ψ are the phase and group angles, respectively. The derivative of group velocity with respect to the group angle ψ is used for calculation. Therefore, it is required to derive a continuous and differentiable function of the group velocity of group angle ψ; here in those lab measurements, ψ equals 28 degrees.

Kumar *et al.*, (2004) approximated a group velocity as a function of group angle for VTI media, which is expressed as:

$$\begin{cases} V_{group}^{-2}(\psi) = a_1 + a_2 \cos^2\psi - a_3 \cos^4\psi, \\ \begin{pmatrix} a_1 \\ a_2 \\ a_3 \end{pmatrix} = inv \begin{pmatrix} 1 & 1 & -1 \\ 1 & \cos^2\psi & -\cos^4\psi \\ 1 & 0 & 0 \end{pmatrix} \begin{pmatrix} V_{group}\left(0^\circ\right) \\ V_{group}(\psi) \\ V_{group}\left(90^\circ\right) \end{pmatrix}. \end{cases} \tag{2.2}$$

By substituting lab measurements $V_{group}\left(0^\circ\right) = V_{pV}$, $V_{group}\left(90^\circ\right) = V_{pH}$, $V_{group}(\psi) = V_{p\Phi}$, into Equation (2.2), I obtain the analytical expression of the group velocity function of the group angle. Then, by substituting the group velocity function into Equation (2.1), I have the function of phase velocities of different angles.

<u>2.2.2 Phase velocity to stiffness mapping</u>

In VTI media, the relationship between the stiffness and phase velocities are given by (Tsvankin, 2001):

$$\begin{cases} C_{11} = \rho V_{pH}^2, \\ C_{33} = \rho V_{pV}^2, \\ C_{55} = \rho V_{sVV}^2, \\ C_{66} = \rho V_{sHH}^2, \\ C_{13} = \dfrac{\sqrt{\left(C_{11}\sin^2\phi + C_{55}\cos^2\phi - 2\rho V_{pH}^2\right)\left(C_{33}\cos^2\phi + C_{55}\sin^2\phi - 2\rho V_{pH}^2\right)}}{\sin\phi\cos\phi}. \end{cases} \tag{2.3}$$

where the phase angle ϕ is the transformed phase angle, which is correspondent to the inclined group angle ψ. By substituting the phase velocities obtained from Equations (2.1) and (2.2) into Equation (2.3), I obtain the stiffness values.

2.2.3 Uncertainty in measurements and strain energy constraints

Besides the direct calculations of the stiffness, I need to incorporate uncertainty because errors are inevitable in lab experiments. Second, strain energy constraints should be satisfied otherwise the medium cannot be physical. The strain energy constraints are (Yan *et al*., 2016):

$$\begin{cases} C_{11} > C_{66}, \\ C_{33} > C_{13}^2, \\ C_{12} > -C_{66}\left(C_{11} - C_{66}\right), \\ \sqrt{\left(C_{11} - 2C_{66}\right)C_{33} + C_{66}^2} - C_{66} < C_{13} < \sqrt{\left(C_{11} - 2C_{66}\right)C_{33}}. \end{cases} \tag{2.4}$$

Because of the lack of repeated measurements, I assume a 5% uncertainty for all measurements. Namely, for each vertical stress, all five measured velocities have 5% uncertainty in their values. Moreover, for the compressional wave velocity $V_{p\Phi}$ that is not measured at 0 nor 90 degrees, I assume its group angle Φ also has a 5% uncertainty. Take the compressional wave velocity measurements at vertical stress equals 4.8 MPa for example, the three blue dots, in Figure 2.5, represent the measured group velocities. For the group velocities at 0 and 90 degrees, the group velocity has a 5% uncertainty in its velocity value, indicated by the blue vertical bars. For the group velocity measured at angle Φ, which is 28 degrees, the measurement has a 5% uncertainty in the measured value of the velocity as well as a 5% uncertainty in the propagation direction, indicated by the vertical and horizontal bars. Note that the value of the group angle Φ is relatively small, thus the horizontal bar which represents measurement angle uncertainty is not obvious in Figure 2.5.

Assuming a bivariate distribution of the possible value of the group velocity and angle within the error bar, I obtain a series of possible group velocity values. Then I transform the possible group velocity combinations to phase velocity based on the theory described in the previous section. Based on the new phase velocities, I calculated the stiffness and check the strain energy constraints described in Equation (2.4). Only those that satisfy the constraints are accepted. In Figure 2.5, I demonstrate the analysis for lab measurements obtained at vertical stress equals 4.8 MPa. The red dots indicate the possible value of the measurements. The thin solid lines are possible group velocity functions. Compared to the curves in Figure 6 and the one group velocity curve of uniaxial effective stress at 4.8 MPa, Figure 2.5 demonstrates all possible group velocity curves that result in stiffness values that satisfy the strain energy constraints.

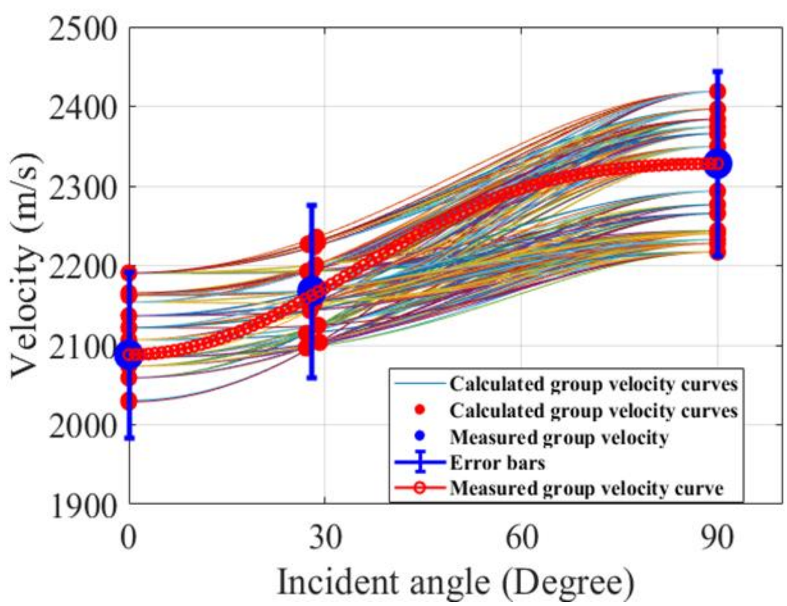

Figure 2.5: Possible group velocity curves.

Each group velocity curve in Figure 2.5 represents a set of stiffness. All possible stiffness values are demonstrated in Figure 2.6, where the error bar indicates the stiffness range resulting from an assumed 5% lab measurement uncertainty. The dots represent possible stiffness values that satisfy the strain energy constraints.

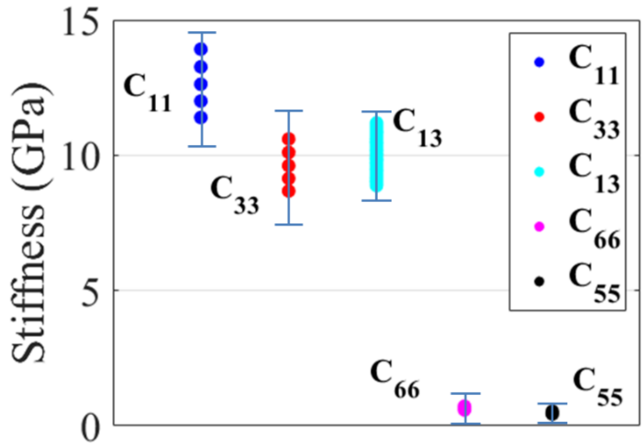

Figure 2.6: Possible stiffness values for the rock sample under a 4.8 MPa vertical stress.

In the same manner, I introduce the uncertainty to all the lab measurements obtained under different uniaxial effective stresses. The final possible stiffness for all stresses is displayed in Figure 2.8.

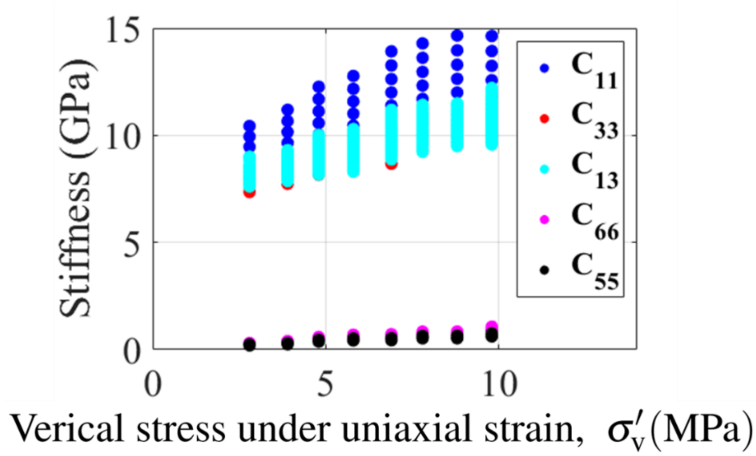

Figure 2.7: Possible stiffness values for all different stress conditions.

In the next step, I apply the maximum likelihood method to obtain a plausible stiffness estimation. More specifically, take the C_{11} from Figure 2.6 as an example. The most likely value is the average of all possible values, which are marked as dots within the error bar. Finally, the most likely stiffness results are shown in Figure 2.8 as the solid lines. The dashed lines in Figure 2.8 indicate the stiffness values calculated directly from the measure group velocities without applying the strain energy constraints nor the maximum likelihood method. The stiffness values represented by the dashed lines are not realistic because of the non-physical trend in C_{13}.

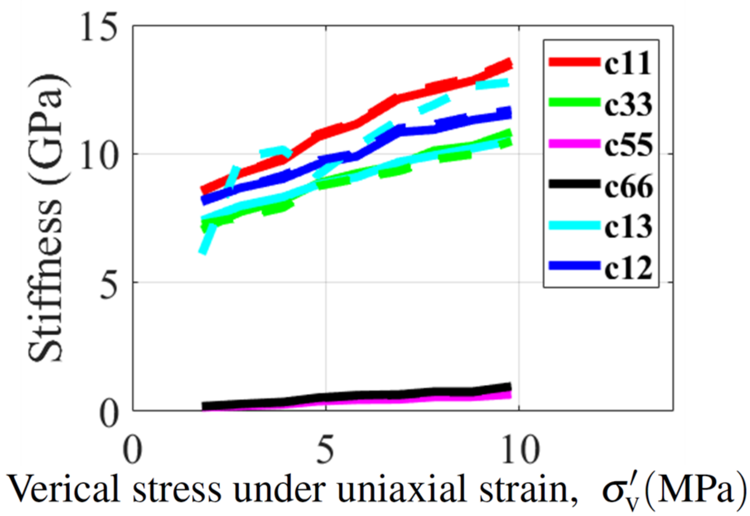

Figure 2.8: Stiffness as a function of stress. Dashed line: direct calculation from lab measurements. Solid line: the most likely results.

2.2.4 Relating stress to stiffness and anisotropy parameters

To obtain the relationship between stress and stiffness, I employ the power law to the stiffness in the form: $a + b\sigma_{\mathrm{v}}^{\prime c}$, where *a*, *b* and *c* are the fitting coefficients. By using the least-squares optimization, I obtain these coefficients for all the 5 stiffness curves. The fitting results are shown in Figure 2.9.

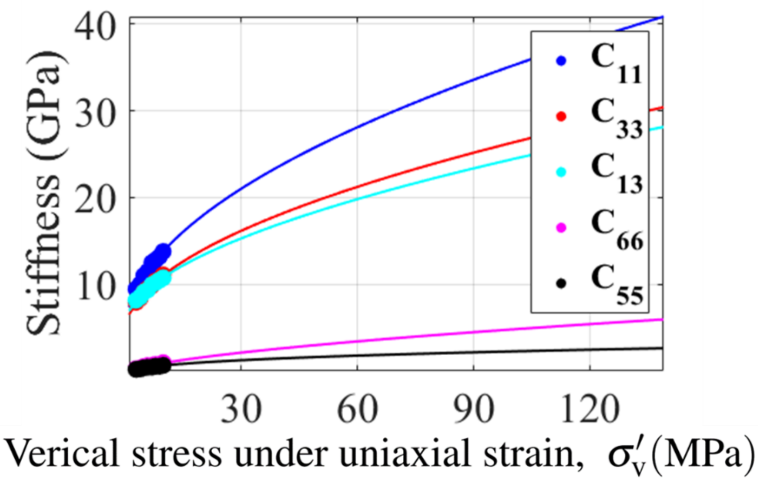

Figure 2.9: Power-law fitting results of stress to stiffness relationship.

Thomsen parameters, which are a straightforward way to describe seismic anisotropy, are given by (Thomsen, 1986):

$$\begin{cases} \varepsilon = \dfrac{C_{11} - C_{33}}{2C_{33}}, \\ \gamma = \dfrac{C_{66} - C_{44}}{2C_{44}}, \\ \eta = \dfrac{\varepsilon - \delta}{1 + 2\delta}, \\ \delta = \dfrac{\left(C_{13} + C_{44}\right)^2 - \left(C_{33} - C_{44}\right)^2}{2C_{33}\left(C_{33} - C_{44}\right)}. \end{cases} \tag{2.5}$$

It is now well established that stress is a major factor that influences seismic velocities including seismic anisotropy. In order to study this problem, uniaxial stress or triaxial stress experiments are generally conducted. Here, I use a set of data from the vertical stress experiment (data courtesy from Tufts University) to demonstrate the workflow of relating stress to stiffness or anisotropy.

2.3 Calculating stiffness parameters for a 2D synthetic model

Ranjpour's (2020) lab measurements were conducted under different vertical stress while strain variation is uniaxial. Here I assume that under the maximum effective principal stress, subsurface media demonstrate the same uniaxial strain behavior. Thus, the vertical stress used in this laboratory experiment is assumed to be identical to the maximum effective principal stress. Based on the stress-stiffness relationship obtained from rock physics analysis of the lab measurements, I calculate the anisotropy model, shown in Figure 2.10 (b), from a synthetic salt basin stress model (Nikolinakou *et al.*, 2018).

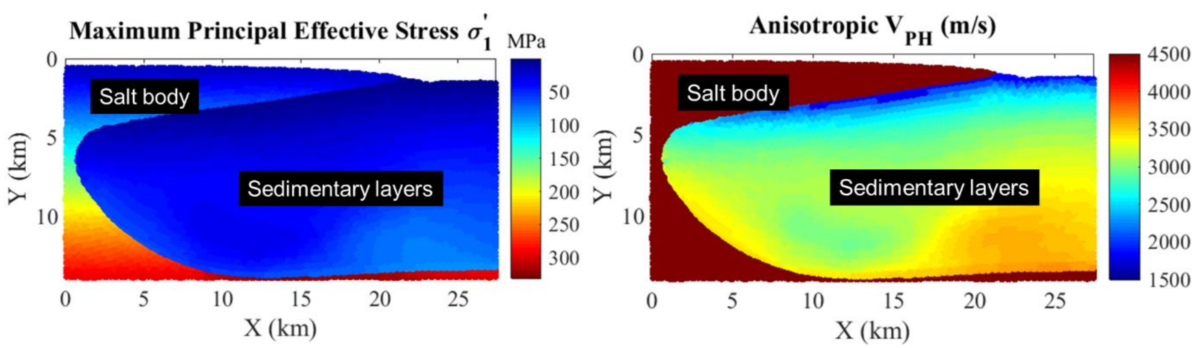

(b) (b)

Figure 2.10: (a) Maximum effective principal stress σ_1' of the synthetic salt basin stress model (Nikolinakou *et al.*, 2018). (b) anisotropy model (horizontal compressional wave velocity) calculated from the stress model.

Furthermore, based on the stiffness results and the Thomsen parameter expressions shown in Equation (2.5), the anisotropy parameters of the Maria model could be readily calculated. The results are shown in Figure 2.11. The tilt angle demonstrated in the bottom right of Figure 2.11 is set to be equal to the angle of the maximum effective principal stress.

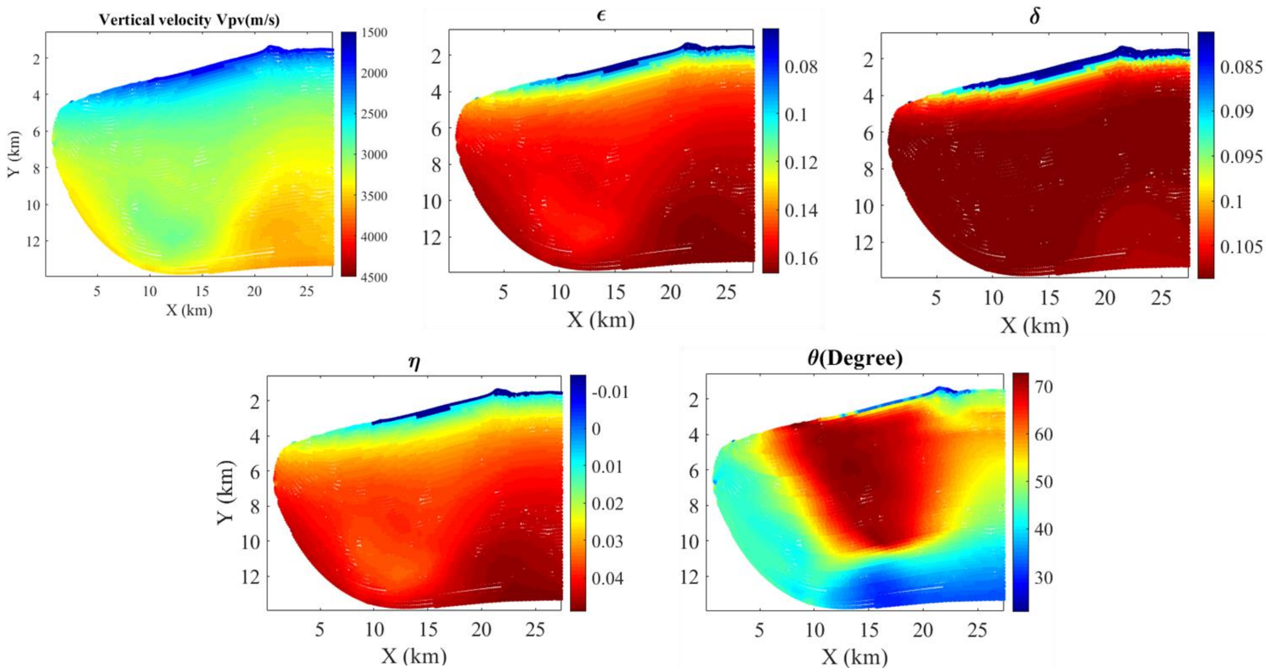

Figure 2.11: Anisotropy parameters for synthetic salt basin stress model of Nikolinakou *et al*., 2018.

2.4 summary

In this chapter, I derive a relationship between stiffness coefficients and stress and apply that relation to derive an anisotropic seismic model from a synthetic stress model of Nikolinakou *et al.* (2018). The lab measurements demonstrate a greater velocity perpendicular to the direction of applied stress, which is explained by the platy clay grain re-alignment process.under the assumption that maximum effective principal stress is related to transversely isotropy (TI) type of anisotropy. With the basic concepts about TI media, I analyze the lab measurements from the rock sample under different vertical stresses and relate those stresses to stiffnesses. Finally, I apply the stress-stiffness relationship to a 2D synthetic stress model and obtain the corresponding stiffness model, which is used for further analysis described in the following chapters.

Chapter 3: Mesh-free seismic forward modeling

Conventionally, the finite-difference (FD) method employs a regular mesh (or uniform grids) to discretize model parameters, which, however, lacks the flexibility for various resolutions. Thus the detailed structures in a model can only be approximated using a large number of grid points. This oversampling problem can be alleviated using a mesh-free discretization, where scattered nodes are distributed suitably with respect to model parameters by changing nodal density accordingly (Fornberg and Flyer 2015). As a consequence, the number of nodes in the computational domain is reduced significantly, which saves significant computational costs. In other words, numerical simulation of wave propagation using the mesh-free finite-difference has the advantages of high computational efficiency and accurate description of irregular boundaries. In addition, this scheme is good at simulating wave propagation in models with large velocity contrasts and complicated model interfaces, such as the salt model.

In this chapter, I explain the discretization scheme of the mesh-free method and the RBF-FD method for calculating spatial derivatives in wave equations. Then, I apply the mesh-free method for acoustic TI media seismic wave simulation, which later will be used for VFSA to test the sensitivity of seismic inversion for stress.

3.1 Mesh-free discretization

Discretizations of model parameters have traditionally relied on structured meshes. Requirements for geometric flexibility, both to conform to irregular geometries and to achieve local refinement in critical areas, have led to increased use of unstructured meshes, often in the form of triangular/tetrahedral elements. In contrast, RBF-generated finite differences (RBF-FD) is a recent and altogether mesh-free approach. It makes it easy to combine geometric flexibility with high levels of accuracy and computational efficiency. It uses scattered nodes with spatially varying density, without forming any associated 'elements' or connectivities between nodes. A key to a successful implementation of RBF-FD methods is being able to very rapidly generate node layouts, as needed for applications such as real-time weather forecasting, tsunami modeling, and seismic imaging. Fornberg and Flyer (2015) proposed the advancing front method for node placing in the mesh-free discretization. The primary advantages of this algorithm are computational speed, algorithmic simplicity, and the quality of the generated node distributions. I will not illustrate the detail of implementing the mesh-free discretization. Readers are referred to Fornberg and Flyer's (2015) paper. In this section, I will illustrate the major advantages of the mesh-free method compared to the conventional FD method.

3.1.1 Accurate representation of irregular interfaces

As mentioned earlier, the conventional FD method discretizes the computation domain with regularly distributed grids, as shown in Figure 3.1. The red cross indicates the FD stencil used to calculate spatial derivatives of wave equations. Figure 3.2 (a) demonstrates a two-layer model with an irregular interface, which is represented as the dashed line. However, the conventional FD method cannot accurately describe an irregular interface, as it is represented by the thick red polyline. The problem that the model interfaces do not align with the Cartesian grid is called the stair-casing problem, which is a non-neglectable source of resolution error.

Figure 3.2 (b) shows the mesh-free discretization scheme for the two-layer model. The irregular interface is accurately described by the unstructured nodes. Figure 3.2 demonstrates that the mesh-free discretization scheme avoids the stair-casing problem by flexibly distributing nodes on the irregular interfaces.

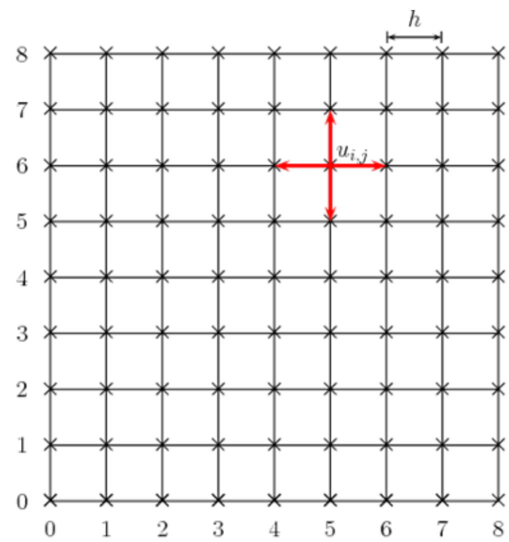

Figure 3.1: Conventional finite difference discretization.

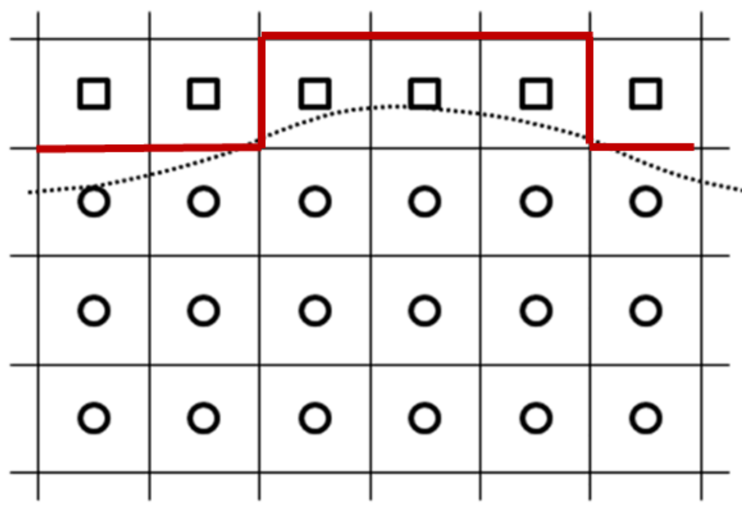

(a)

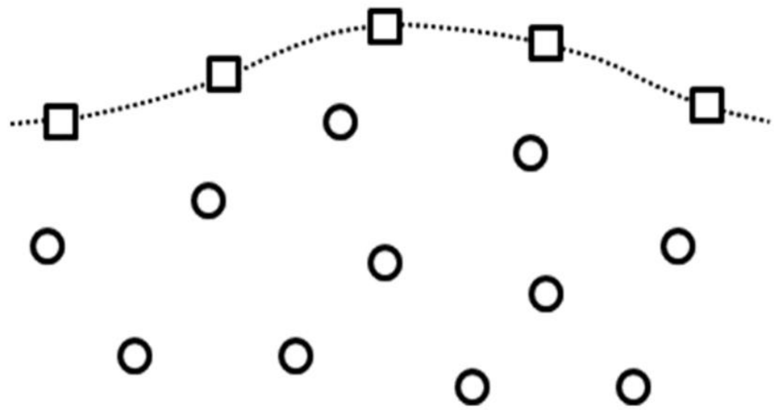

(b)
Figure 3.2: Discretization schemes for a two-layer model with an irregular interface. (a) conventional finite difference method. (b) mesh-free method.

3.1.2 Adaptive distribution of mesh-free nodes

For heterogeneous models, different resolutions are required for different parts of the model to adequately discretize them. For example, a lower resolution is required for a high-velocity zone while a higher resolution is required for a low-velocity zone. However, in the conventional FD method, the meshing interval is chosen globally and is constant throughout the computation domain. The constant resolution for different parts of a model leads to the redundancy of modeling accuracy, also called the over-sampling problem. On the other hand, mesh-free discretization is a scheme that allows local modification of node configurations by simply placing more nodes in regions where needed and removing them from regions that are already overpopulated. Moreover, this scheme can flexibly distribute nodes without a computationally expensive meshing process. Therefore, mesh-free discretization can save plenty of nodes through distributing nodes adaptively to irregular boundaries and model parameters (Li *et al.*, 2017). This means, in seismic wave simulation using the mesh-free discretization, for lower velocity areas or heterogeneous bodies such as multi-scale structures or interfaces with high contrast between physical parameters, node distance could be small enough to assure sufficient sampling to capture the model features.

In my work, the node distance is governed by a linear relationship with respect to the local velocity. The equation is expressed by:

$$r = \frac{v_{\max} - v_{\min}}{r_{\max} - r_{\min}}(v - v_{\min}) + r_{\min}, \tag{3.1}$$

where $v_{\max}$ and $v_{\min}$ are the maximum and minimum velocities, respectively. $r_{\max}$ and $r_{\min}$ are the maximum and minimum node distances, respectively.

Figure 3.3 displays a heterogeneous model with an irregular interface and an elliptical low-velocity anomaly under the interface. Figure 3.4 is the mesh-free discretization of this model. Note that this model is non-rectangular, and the irregular boundaries are discretized by mesh-free nodes. Figure 3.5 shows the nodal distributions of the red square regions shown in Figure 3.4. These figures demonstrate the flexibility of the mesh-free discretization scheme and its accuracy in describing irregular interfaces. As shown in Figure 3.4, the node distances in different velocity zones are linearly related to the local velocities. Figure 3.5 demonstrates that the mesh-free method could accurately describe the non-Cartisen interfaces. This example shows that compared to the conventional FD method, the mesh-free discretization method has the advantages of overcoming the stair-casing problem and the over-sampling problem.

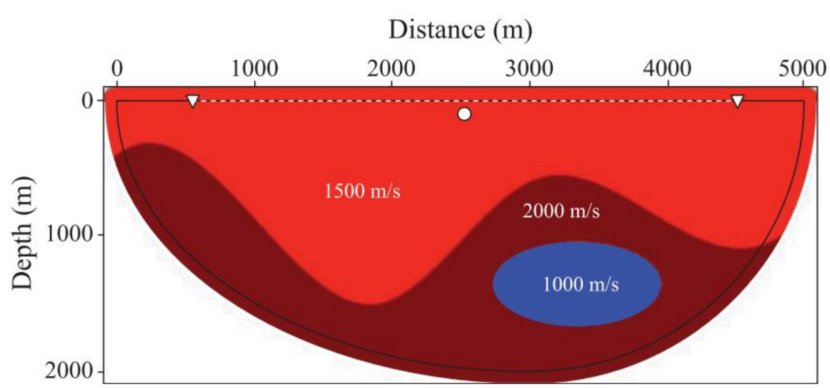

Figure 3.3: A heterogeneous model with a piecewise smooth boundary which is combined by a flat edge and a curved edge. The model contains an irregular interface and an elliptical low-velocity anomaly under the interface. The solid black line represents the piecewise boundary. (Li *et al.*, 2017)

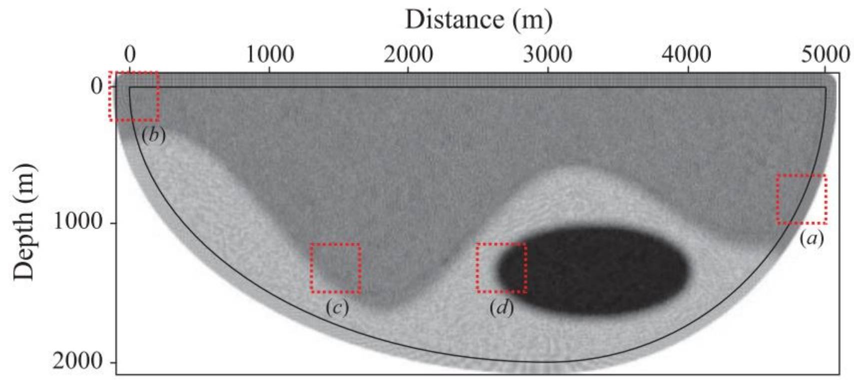

Figure 3.4: Overall nodal distribution for the heterogeneous model shown in Figure 3.3. The dashed squares indicate specific regions where scattered nodes are placed to fit the boundary ((a) and (b)) or the model structures ((c) and (d)). Their corresponding nodal distributions in zoom view are shown in Figure 3.5. (Li *et al.*, 2017)

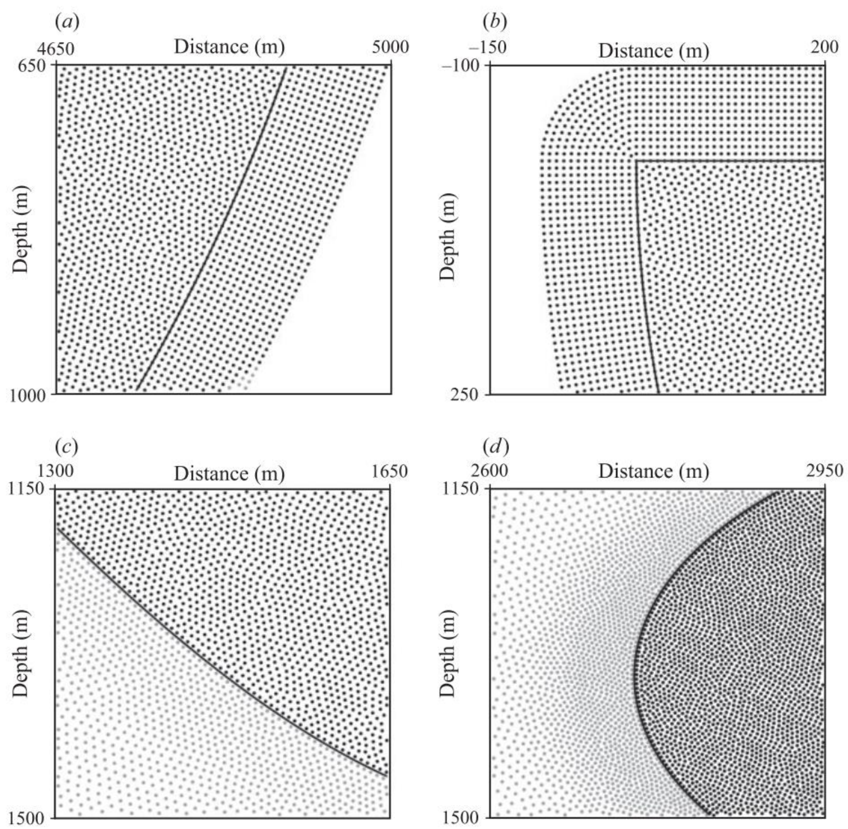

Figure 3.5: Nodal distributions of the dash square regions shown in Figure 3.4. (Li *et al.*, 2017)

3.2 Mesh-free discretization RBF-FD anisotropy seismic modeling

3.2.1 RBF-FD for calculating spatial derivatives

In the conventional FD method, the stencil for calculating spatial derivatives is shown in Figure 3.1 as the red cross. In the mesh-free method, the RBF-FD method is utilized to approximate the spatial derivatives. Figure 3.6 is an illustration of the quasi-uniform nodal distribution based on mesh-free discretization. As shown in this figure, the spatial derivatives at the red node are evaluated through the values on the nearby blue nodes.

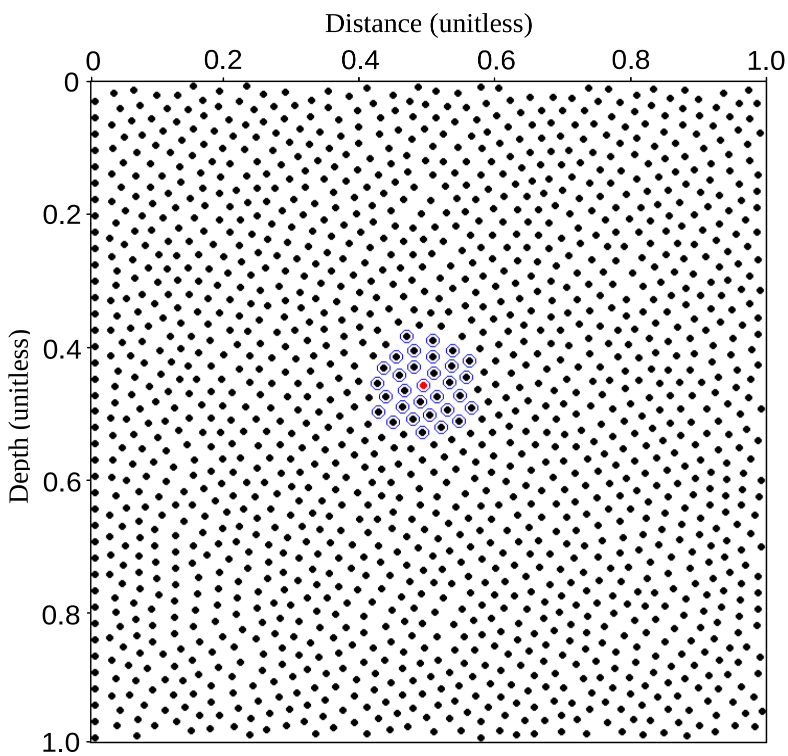

Figure 3.6: Illustration of quasi-uniform nodal distribution. The small open circles indicate the FD stencil with M = 30, in which the little red dot represents the center node of the stencil.

In mesh-free discretization, the spatial derivatives need to be taken special care of, because the stencil used to compute derivatives is usually not regular. Many techniques have been proposed to calculate partial derivatives over scattered nodes. RBF-FD is one such method, which has gained significant popularity due to its efficiency and computational speed as compared to other mesh-free methods. Recently, the combination of polyharmonic spline RBFs augmented with high-order polynomials (PHS+Ploy) in the RBF-FD formulation has demonstrated several merits such as significant robustness even for single-sided stencils, simple formulation free from tuning the shape parameter, and the potential of maintaining the accuracy for large-sparse linear systems (e.g., Fornberg and Flyer, 2015; Bayona *et al.*, 2017, Mishra *et al.*, 2019). The order of convergence for the PHS+Poly RBF-FD is mostly dependent on the highest degree of the augmented polynomials, which also dictates the stencil size. This feature makes it possible to adapt different stencil sizes for different fill distances while keeping the order of convergence consistent for the entire computational domain. Different variations of RBF-FD methods have been recently shown to work effectively for seismic modeling (e.g., Martin *et al.*, 2015; Berljavac *et al.*, 2020).

The RBF-FD is a method that the approximation of an operator L (such as the first-order or the second-order derivatives) at the central node x_c is obtained as a weighted sum of function values on the central node and its neighboring *(M - 1)* nodes, which can be expressed as (Martin *et al.*, 2015):

$$Lf(x)\big|_{x=x_c} \approx \sum_{i=1}^{n} w_i f\left(x_i\right), \tag{3.2}$$

where a_i is the weighted coefficient of the i^{th} node and $\phi(\| x - x_k\|)$, $k = 1, 2, 3\ldots, M$ are radially symmetric functions. Here I employ the PHS-RBF, namely $\phi(r) = r^{2m+1}$, where m, an odd number greater than 3, is the power of the PHS. By solving Equation 3.2, the weight a_i for approximating operator L can be obtained. Moreover, by including additional polynomials into RBF-FD and adding matching constraints, the RBF-FD can defeat the stagnation error in convergence rate because the order of convergence is determined by the highest degree of the augmented polynomials. For instance, when including Taylor monomials (1, x, y), the matrix form of equation (3.2) is (Larsson *et al.*, 2013):

$$\begin{bmatrix} \phi(\|x_1-x_1\|) & \phi(\|x_2-x_1\|) & \cdots & \phi(\|x_M-x_1\|) & 1|_{x_1} & x|_{x_1} & y|_{x_1} \\ \phi(\|x_1-x_2\|) & \phi(\|x_2-x_2\|) & \cdots & \phi(\|x_M-x_1\|) & 1|_{x_2} & x|_{x_2} & y|_{x_2} \\ \vdots & \ddots & \ddots & \vdots & \vdots & \vdots & \vdots \\ \phi(\|x_1-x_M\|) & \phi(\|x_2-x_M\|) & \cdots & \phi(\|x_M-x_M\|) & 1|_{x_M} & x|_{x_M} & y|_{x_M} \\ 1|_{x_1} & 1|_{x_2} & \cdots & 1|_{x_M} & 0 & 0 & 0 \\ x|_{x_1} & x|_{x_2} & \cdots & x|_{x_M} & 0 & 0 & 0 \\ y|_{x_1} & y|_{x_2} & \cdots & y|_{x_M} & 0 & 0 & 0 \end{bmatrix} \begin{bmatrix} a_1 \\ a_2 \\ \vdots \\ a_M \\ a_1^* \\ a_2^* \\ a_3^* \end{bmatrix} = \begin{bmatrix} L\phi(\|x-x_1\|)|_{x_c} \\ L\phi(\|x-x_2\|)|_{x_c} \\ \vdots \\ L\phi(\|x-x_M\|)|_{x_c} \\ L(1)|_{x_c} \\ L(x)|_{x_c} \\ L(y)|_{x_c} \end{bmatrix}, \quad (3.3)$$

For a certain partial derivative operator L, solving Equation (3.3) yields the correspondent weights, and then disregards the auxiliary weights a_1^*, a_2^*, and a_3^*. The results a_i, where $i = 1, 2, 3\ldots, M$, corresponding to the i^{th} nodes in the stencil, can be used as weights to compute the partial derivative.

3.2.1 RBF-FD for mesh-free modeling of acoustic TI media

Seismic inversion is a technique used to obtain high-quality subsurface properties. Despite the elastic nature of the Earth, the anisotropic acoustic wave equation is typically used to model wave propagation in seismic inversion. This simplification is essential for being efficient and can avoid cross-talk and other multi-parameter elastic seismic inversion. Duveneck *et al.* (2008) and Xu *et al.* (2016) proposed a two dimensional (2D) an accurate acoustic TI media wave equation:

$$\begin{cases} \dfrac{1}{V_{pH}^2}\dfrac{\partial^2 U_H}{\partial t^2} = (1+2\varepsilon)H_1 U_H + \sqrt{(1+2\delta)}H_2 U_v, \\ \dfrac{1}{V_{pH}^2}\dfrac{\partial^2 U_V}{\partial t^2} = \sqrt{(1+2\delta)}H_1 U_H + H_2 U_V, \end{cases} \quad (3.4)$$

where the interim terms are expressed by:

$$\begin{cases} H_1 = \cos^2\theta\cos^2\varphi\frac{\partial^2}{\partial x^2} + \sin^2\theta\frac{\partial^2}{\partial z^2} + \sin 2\theta\cos\varphi\frac{\partial^2}{\partial x\partial z}, \\ H_2 = \sin^2\theta\cos^2\varphi\frac{\partial^2}{\partial x^2} + \cos^2\theta\frac{\partial^2}{\partial z^2} - \sin 2\theta\cos\varphi\frac{\partial^2}{\partial x\partial z}. \end{cases} \tag{3.5}$$

In Equations (3.4), U_H and U_v are the particle displacements in horizontal and vertical directions, respectively. V_{pH}, ε and δ are the Thomsen parameters that characterize media anisotropy. In Equation (3.5), θ and φ are the tilted and azimuth angles of the TI media, where θ is assumed to be identical to the angle of the maximum effective principal stress, φ is 0 for 2D media.

3.3 Numerical example of mesh-free discretization RBF-FD anisotropy seismic modeling

Here I apply the mesh-free RBF-FD seismic forward modeling for the acoustic TI media shown in Figure 2.11. Figure 3.7 are the results for isotropic media modeling and anisotropic media, respectively. As shown in Figure 3.7, the source is placed in the center of the model. And the nodes are adaptively distributed according to local velocity. Those results prove the validity of acoustic anisotropic modeling with the mesh-free RBF-FD method.

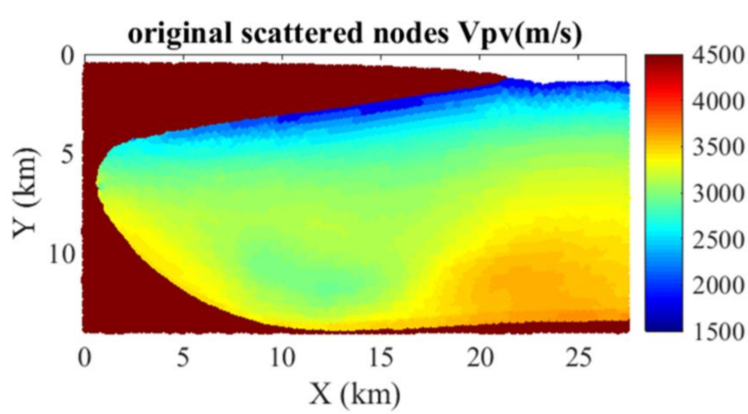

(a)

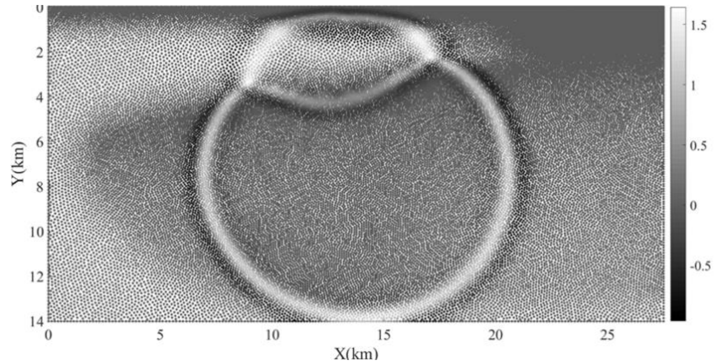

(b)

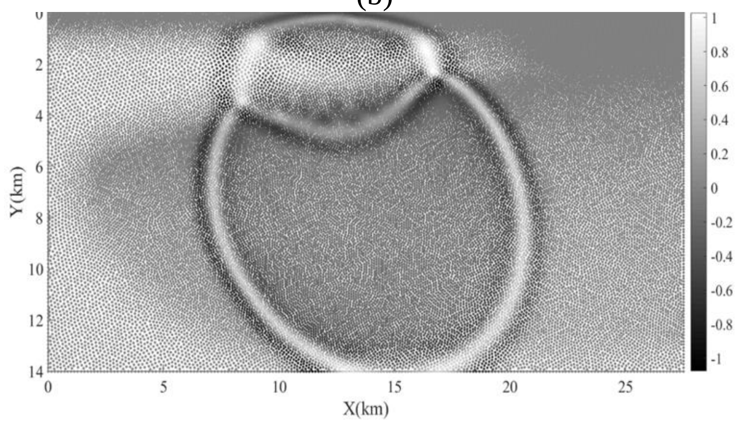

(c)

Figure 3.7: Mesh-free RBF-FD modeling results. (a) isotropic model correspondent to the synthetic salt basin. (b) isotropic media modeling snapshot. (c) acoustic TI media modeling.

Then I carry out another seismic modeling on this model, where I put the source at the center on the surface and the receiver line is buried 200 m below the surface. Figure 3.8 shows the shotgathers obtained from mesh-free RBF-FD simulation for isotropic (a) and the anisotropic cases (b). Figure 3.9 displays the difference between the two shotgathers. These results show the effect of stress on seismic response.

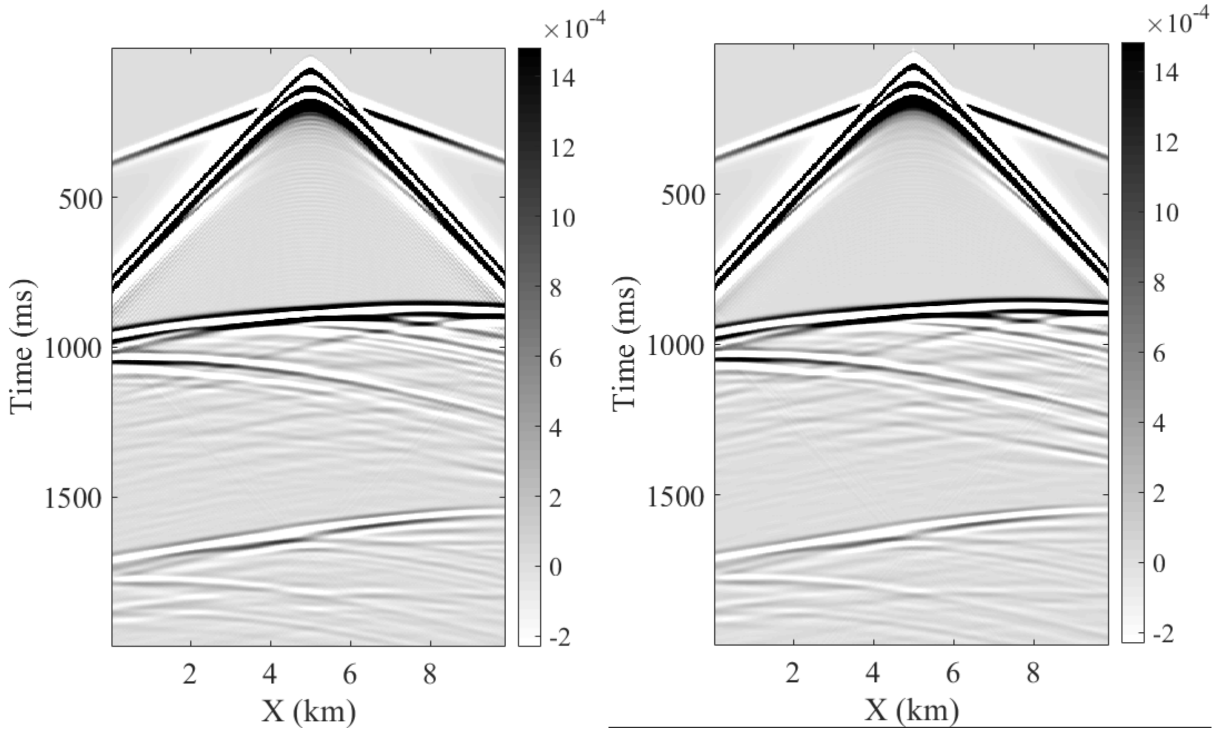

(a) (b)

Figure 3.8: Mesh-free RBF-FD modeling shotgathers. (a) isotropic media. (c) acoustic TI media.

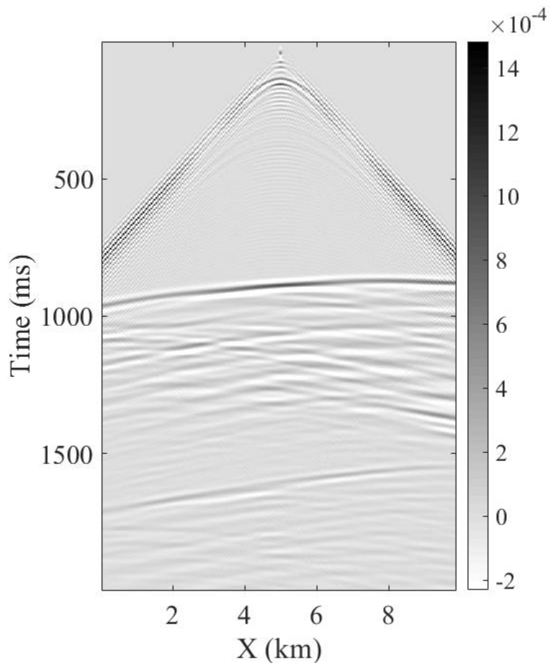

Figure 3.9: Difference between shotgathers of isotropic media and acoustic TI media. The difference between direct waves before 700 ms is caused by numerical dispersion. The difference between reflected waves is caused by stress-induced anisotropy.

3.4 Summary

In this chapter, I illustrate the advantages of mesh-free RBF-FD seismic modeling, which are an accurate representation of irregular interfaces and flexible nodal distribution. Then I apply this method to acoustic TI media simulation. At last, I compare the results of the isotropic and anisotropic simulations. The difference indicates the effect of stress on seismic response.

Chapter 4: Seismic inversion for stress

In Chapter 2, I derive a relationship between stress and stiffness using laboratory measurements of one rock sample. However, before applying seismic inversion for stress, it is important to investigate the feasibility of inverting for stresses from reflection seismic data. In this chapter, I test if it is possible to invert for stress information from seismic data based on the stress-stiffness relationship described in Chapter 2.

4.1 Seismic inversion

Despite the elastic nature of the Earth, the acoustic wave equation is typically used for seismic inversion. In this work, in order to reduce the complexity of stress inversion, I will focus on acoustic anisotropic media, where anisotropy is induced by stress, and the stress stiffness relationship is assumed to be identical to the one obtained from laboratory measurements. Therefore, anisotropic parameters of the acoustic TI media can be expressed by the magnitude and angle of the maximum effective stress. This chapter introduces a new acoustic TI wave equation, where, compared to the conventional ones, the seismic parameters are substituted by the magnitude and angle of the maximum effective stress. This makes it convenient to directly invert for stress information from the seismic records. Furthermore, in order to test the sensitivity of this seismic inversion for stress, I employ a global optimizing method to avoid being trapped in local minima, and I test this inversion on some simple models.

4.2 Stress inversion from seismic data

4.2.1 Stress based-acoustic TI media wave equation

Based on the stress-induced anisotropy theory, I assume that the tilt angle is identical to the angle of the maximum effective stress. Moreover, according to the stress stiffness relationship obtained from Chapter 2, the Thomsen parameters can be expressed by the magnitude of the maximum effective principal stress. Therefore, the acoustic TI wave Equation (3.4) can be re-written as:

$$\begin{cases} \dfrac{1}{\left(a_{11}+b_{11}\sigma_1^{'c11}\right)^2}\dfrac{\partial^2 U_H}{\partial t^2} = \left[1+\dfrac{\left(a_{11}+b_{11}\sigma_1^{'c11}-a_{33}+b_{33}\sigma_1^{'c33}\right)}{a_{33}+b_{33}\sigma_1^{'c33}}\right]H_1U_H+\sqrt{(1+2\delta)}H_2U_v, \\ \dfrac{1}{\left(a_{11}+b_{11}\sigma_1^{'c11}\right)^2}\dfrac{\partial^2 U_V}{\partial t^2} = \sqrt{(1+2\delta)}H_1U_H+H_2U_V, \end{cases} \tag{4.1}$$

where a, b, and c with the subscripts are the coefficients obtained from power-law fitting of the stress to stiffness, shown in Figure 2.9. Note that the parameter δ is not substituted by the stress variable, because δ is a very small value and insensitive to seismic inversion. In practice, δ is obtained from well logging interpolation and is kept constant during seismic inversion.

4.2.2 Very fast simulated annealing

The goal of seismic inversion is to estimate subsurface media parameters from observed seismic data. Based on the stress-stiffness relationship, I develop a simplified stress estimation workflow as shown in Figure 4.1. In this workflow, synthetic data are generated from an assumed model and then compared with the observed data. If the misfit between the synthetic data and the observed data is very small, the assumed model is accepted as the solution. Otherwise, the model is updated and the synthetics are recomputed and compared to the observations again. This loop is repeated until the misfit reaches an acceptable minimum value or the maximum iteration is reached. The forward modeling part is carried out via the mesh-free RBF-FD method. The most crucial part of this workflow is updating the stress model, also called optimization.

Optimization methods are broadly classified into two categories: local optimization and global optimization. The local optimization methods utilize local information such as the local gradient of the data misfit to compute the update. Local optimization methods are widely used due to their higher convergency rate, but they suffer from being trapped in local minima (Yao *et al.*, 2018). On the other hand, the global optimization methods use global information to compute the model update. Their convergency rate is generally much lower than the local optimization methods. The global optimization methods' low convergence rates make it hard to deal with very large models, especially in 3D.

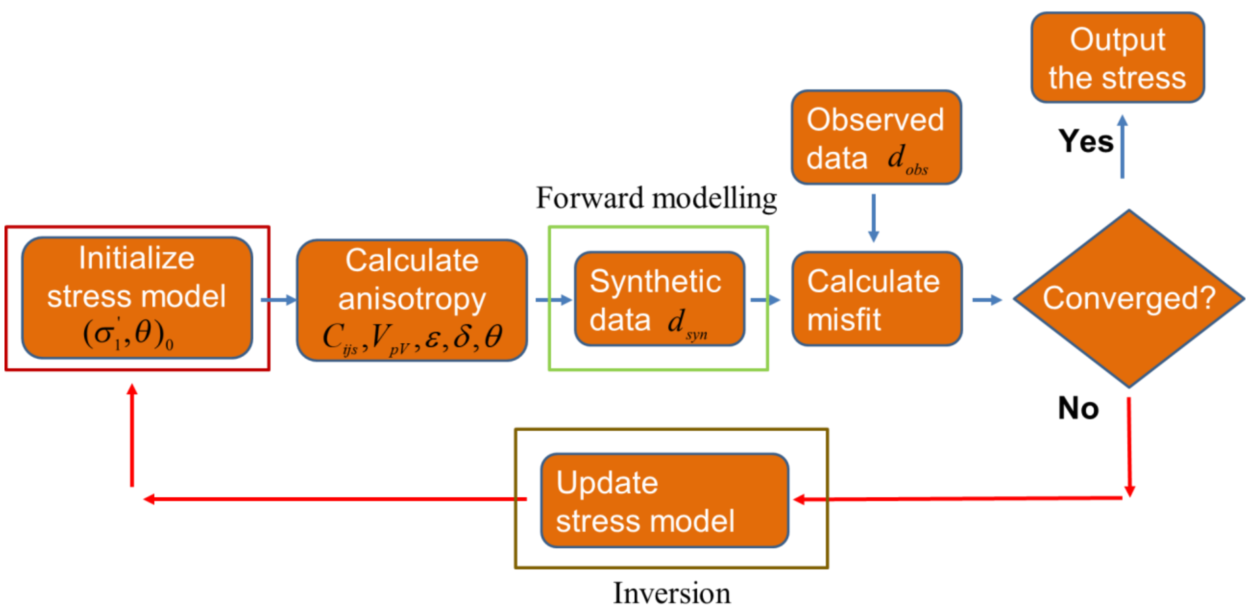

Figure 4.1: simplified workflow of seismic inversion for stress.

The simulated annealing algorithm (SA) is a global search method invented to avoid local minima. It was first proposed by Kirkpatrick *et al.* (1983) as it is analogous to the natural process of crystal annealing when a liquid cools to a solid state. The main shortcomings of this algorithm are its slow convergence and difficulty in the tuning of its parameters. It is claimed that newer versions of fast SA (FSA) and very fast SA (VFSA) have resolved these problems (e.g., Sen and Stoffa, 1995; Datta *et al*., 2018).

Very fast simulated annealing (VFSA) (Ingber and Rosen, 1992; Sen and Stoffa, 2013) is a global optimization algorithm inspired by the physical process of annealing. It does not require a good starting model to converge to the global minimum and is ideally able to start from any random position in the search space.

The VFSA, like the physical process of heat bath annealing, aims to minimize the energy (error) of a system. At every iteration, a dimensionless parameter *T*, which is called the temperature, dictates the perturbation and acceptance of the candidate models. The major improvement in VFSA compared to SA is that the new model is drawn from a temperature-dependent Cauchy-like distribution centered on the current model, which is described in Equations (4.2), (4.3), and (4.4). This method usually starts with a high temperature evaluating a random model and perturbs it using a temperature-dependent Cauchy distribution given by

$$m_{new} = m_{old} + y_i(m_{max} - m_{min}), \tag{4.2}$$

where m_{old} is the previous candidate model, here, the model represents target subsurface seismic parameters, here it refers to the magnitude and angle of the maximum effective principal stress. m_{new} is the new candidate model, m_{max} is the max value of the search space, m_{min} is the minimum value of the search space, and y_i is given by

$$y_i = sgn(u - 0.5)T_i[(1 + T_i)^{2u-1} - 1)], \tag{4.3}$$

where T_i is the temperature at the i^{th} iteration, *sgn* is the signum function, and *u* is a random number in (-1,1). This perturbation function in equation (4.4) is what makes VFSA "fast" compared to conventional simulated annealing (SA) (Metropolis et al., 1953). Although the perturbation function in SA chooses new models from the entire search space at every iteration, VFSA has a Cauchy-like distribution that shrinks the perturbation amplitude as the temperature reduces. The cost function value of the new model E_{new} here is the difference between the synthetic data and the observed data, and m_{new} is accepted as the solution if $E_{new} \leq E_{old}$, where E_{old} is the cost function value for the old model. When $E_{new} \geq E_{old}$, m_{new} is accepted with a probability P_i given by

$$P_i = e^{-\frac{\Delta E}{T_i}}, \tag{4.4}$$

where P_i is the probability of accepting worse solutions, $\Delta E = E_{new} - E_{old}$, is the difference in cost between the current and perturbed model, and T_i is the temperature at the ith iteration (Metropolis *et al*., 1953).

The probability of accepting worse solutions using this criterion gradually diminishes with decreasing temperature meaning that the acceptance of worse solutions reduces by the decreasing temperature. This enables model exploration at higher temperatures and gradually switches to model exploitation as the temperature reduces. The steps are repeated at each iteration with lowering temperatures to obtain an optimum model. To ensure that the algorithm performs optimal model exploration, a few forward evaluations are performed in the same iteration/temperature. The total number of forward evaluations is given by the product of the number of iterations and runs per temperature.

Given its advantages in avoiding local minima and relatively faster convergence rate and more stable convergence path, VFSA is used in this work to compute the model update.

4.3 Sensitivity analysis of seismic inversion for stress

In the sensitivity analysis experiments reported here, the observations are generated from known models. These synthetic data are used in VFSA which starts with a random model to investigate if the algorithm can find the known true model.

Here, I utilize a two-layer model and a model with continuous change in stress, to test the feasibility of stress inversion from seismic data. As shown in Figure 4.2, the two-layer model consists of two homogenous layers each with a different stress magnitude and direction. On the other hand, the stress increases with depth using a linear trend. While model 1 contains reflections from the discontinuity, model 2 contains turning ray arrivals. Note that complex structural models can be built using these two simple models as bases.

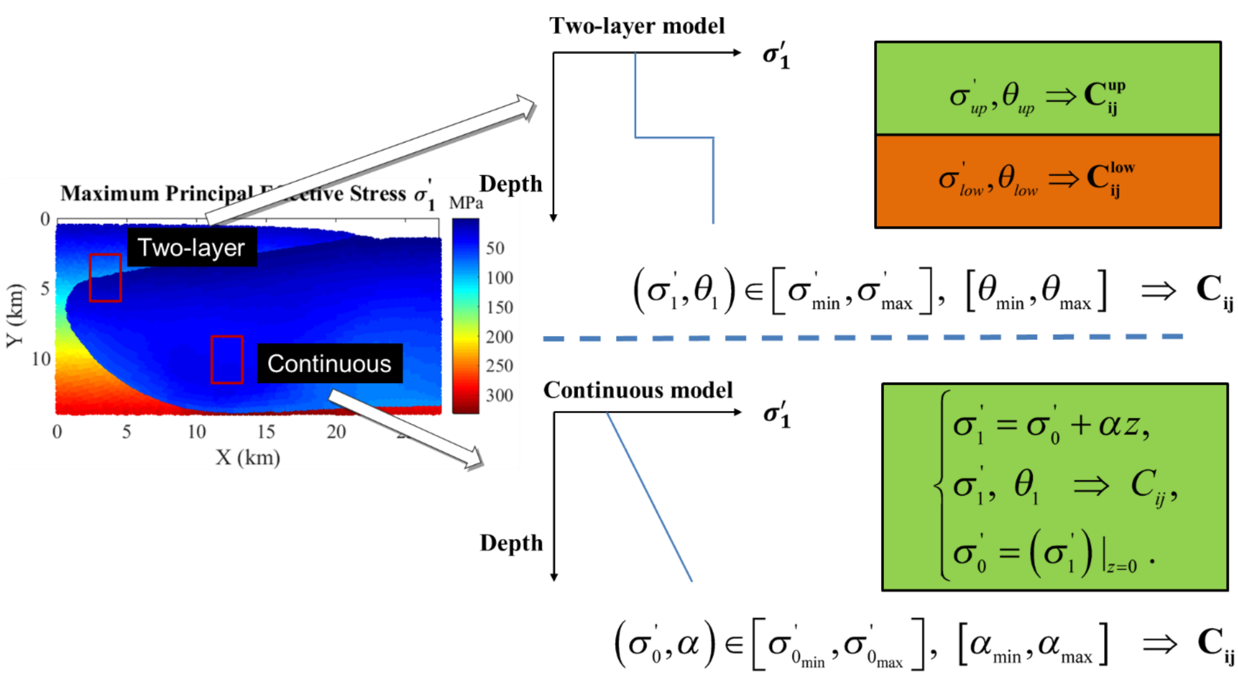

Figure 4.2: Illustration of how to represent a complicated model with a sum of simple models.

First, I examine the sensitivity of changes in stress values in seismic data. For this purpose, I generate a series of synthetic shotgathers with changing stress values. I carry out a sensitivity test using these gathers as follows:

- Use the shot-gather from model 1 or model 2 as the observation (field seismic data).
- Compute the mean square difference (misfit) between each of the shot-gathers (computed for different stress models) and the observation.
- Generate a contour plot of the difference.

4.3.1 Model 1: Two-layer model with a discontinuous change of stress

Figure 4.3 demonstrates the layout of the two-layer model, where the stress parameters are known. The only two unknowns are the magnitude and angle of the upper layer stress. The search ranges of the upper layer stress parameters are shown at the bottom of Figure 4.3. Figure 4.4 displays the shotgathers of the true model, the starting model, and their difference. The shotgathers of the true model is referred to as the observation, as it is regarded as the observation from the field survey. I generate a contour plot of the difference between the synthesized seismic data and the observation. Each cell on the contour map represents the value of the root mean square difference between the observation and the seismic data obtained from one stress state. As shown in Figure 4.5 (a), the red ellipse marks the difference between the seismic data, which is generated by assuming the upper layer stress state to be 3.84 MPa and 27 degrees, and the observation. Figure 4.5 (a) also indicates the true stress state, which is located at the cell with a minimum error value. However, the exhaustive search is not practical nor accurate (the true model is not necessarily located at the sampling point). To efficiently search for the true stress state, I employ the VFSA method. The error as a function of iteration is displayed in Figure 4.5 (b). The red dots in Figure 4.5 (a) and (b) are one-to-one mappings, which indicates the convergency path of the VFSA method. Figure 4.5 indicates that the exhaustive search took 400 evaluations, while the VFSA converged to the true value at around 30 iterations. Moreover, the exhaustive search is not practical nor accurate, because the true model is usually not on the sampling point. Note that, in this simple model exercise, due to the simplicity of this model, only one shot gather is used. However, in multi-shot cases, this method should be paralleled to use all shotgathers.

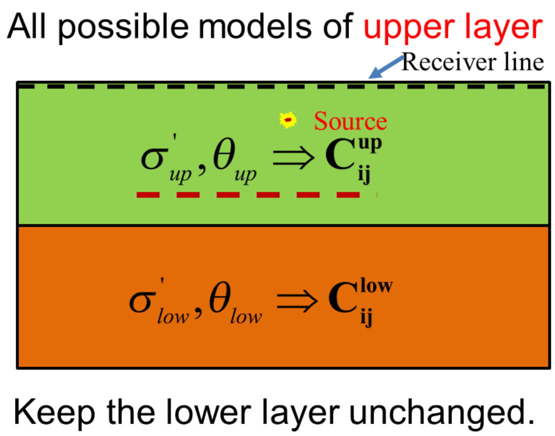

$$\begin{cases} (\sigma'_{up}, \theta_{up}) \in [3.84 \text{ MPa}, 5.76 \text{ MPa}],\ [24^\circ, 36^\circ], \\ \sigma'_{low} = 2.0 \text{ MPa},\ \theta_{low} = 30^\circ. \end{cases}$$

Figure 4.3. The two-layer model with fixed lower layer stress.

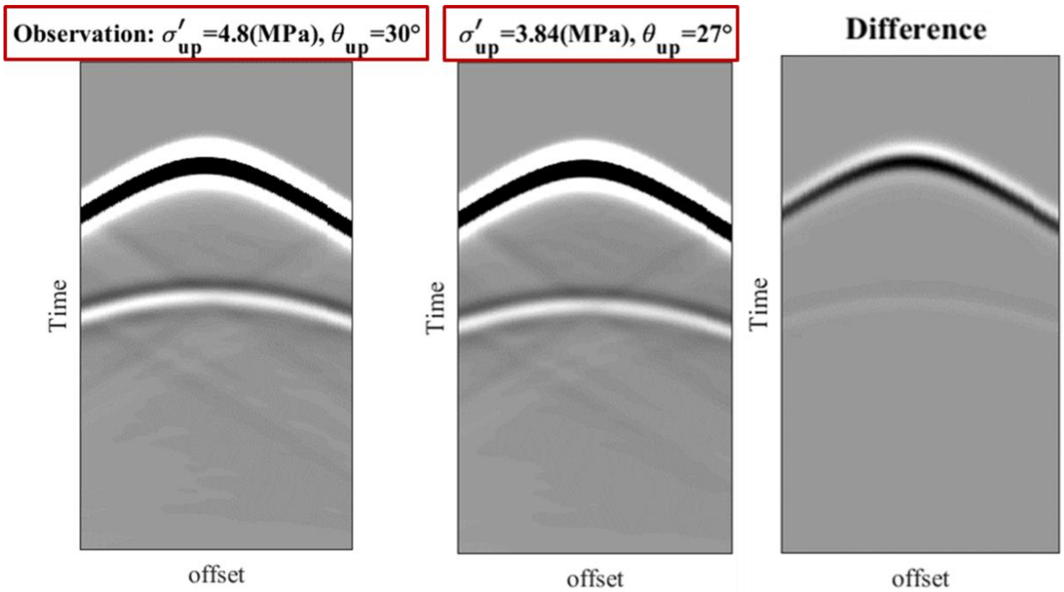

(a) (b) (c)

Figure 4.4. (a) Seismic data from the true stress state (observation). (b) seismic data from a different stress state (guess). (c) the difference between the two seismic data.

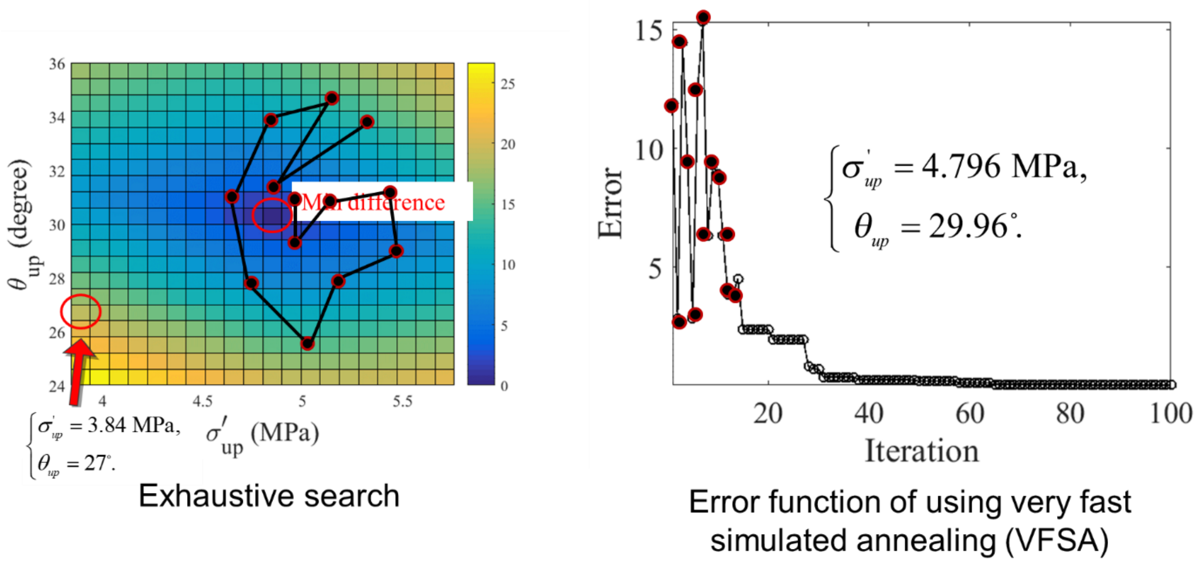

(a) (b)

Figure 4.5. Results for the two-layer model inversion. (a) the contour of the seismic data difference with the observation. (b) error function of using the VFSA method.

4.3.1 Model 2: One-layer model with a continuous change of stress

Next, I carry out the exercise on the continuous model, where the stress varies linearly with respect to depth, as shown in Figure 4.6. So the unknowns are the starting stress, the stress value at the top of this model, and the stress gradient, the stress change per unit depth. Here I set the reference model with starting stress of 2.8 MPa and the stress gradient to be 0.01 MPa/m. The tilt angle is fixed to be 30 degrees for this TI media. I conduct the same seismic inversion as for the two-layer model.

Figure 4.7 demonstrates the contour of the root mean square difference between the synthesized seismic data and the observation for the continuous model. The difference between Figures 4.5 and 4.7 is that in Figure 4.7 (a), the x- and y-axis are the starting stress and the stress gradient. Figure 4.7 (b) shows the error curve of the VFSA for this continuous model. Figure 4.7 (a) indicates for stress inversion of the starting stress and the stress gradient, the error contour is flatter than the one in Figure 4.5 (a). Therefore, it takes more iterations to converge to the final result, as shown in Figure 4.7 (b).

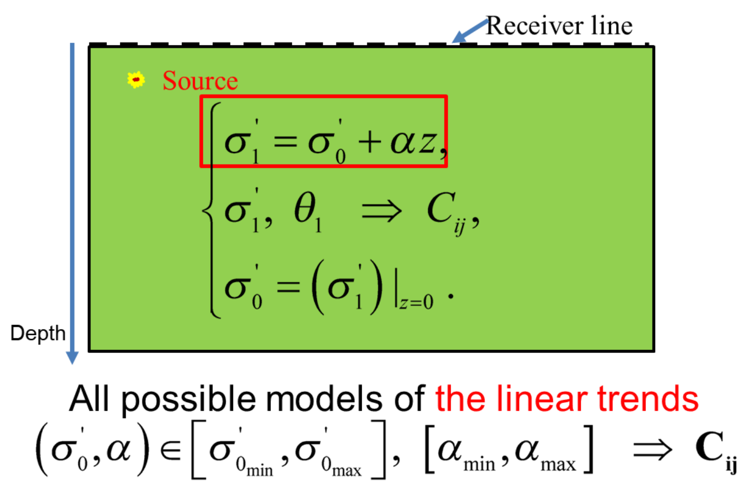

Figure 4.6: The continuous model with unknown starting stress and stress gradient.

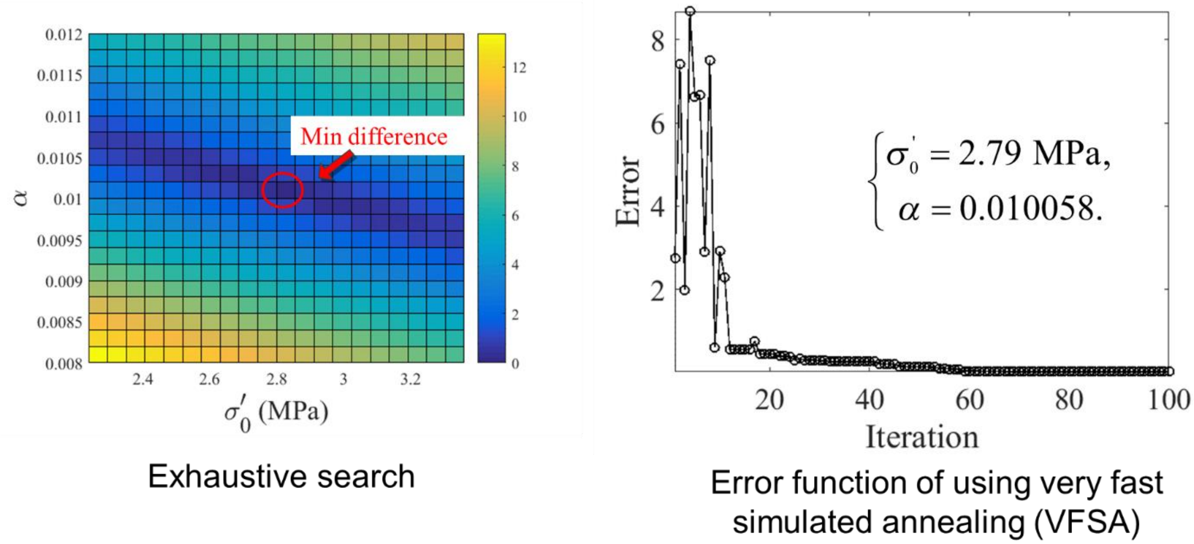

(a) (b)

Figure 4.7. Results for the continuous model inversion. (a) the contour of the seismic data difference with the observation. (b) error function of using the VFSA method.

4.4 Summary

In this chapter, I have demonstrated the feasibility of predicting stress from seismic data through synthetic experiments on two simple models. Moreover, complex structural models can be built using these two simple models as bases, as shown in Figure 4.2. Therefore, these works demonstrate the feasibility of seismic data-based stress prediction.

Chapter 5: Conclusions and future work

5.1 Conclusions

First, this thesis analyzes the lab measurements to obtain the maximum likelihood stress to stiffness relationship. In this step, I assume the subsurface media to be transversely isotropic, then transform the measured group velocities to the phase velocities to calculate stiffness. Next, I utilize the maximum likelihood method to mitigate the influence of measurements error. At last, I used the power law to extrapolate the stress-stiffness relationship to a higher stress range.

The second step of this thesis is applying the mesh-free method to acoustic TI media seismic forward modeling. First, I illustrate the advantages of mesh-free discretization compared to the conventional FD methods. Then, I explain the RBF-FD method which is used for solving the mesh-free seismic wave equation. At last, I apply this method to an anisotropic model and simulate the propagation in anisotropic TI media.

The last step is a sensitivity analysis of the seismic inversion for stress. First, introduce the VFSA algorithm. Then I applied the seismic inversion on some simple models. The results demonstrate the feasibility of predicting stress from seismic data.

5.2 Future work

Future work may include implementing seismic inversion for stress with full waveform inversion (FWI), which is a local optimization method. Seismic stress inversion based on FWI might be possible to estimate stress from complicated models.

Appendix A: Nomenclature table

Symbol	Name	Dimensions
C_{ij}	Stiffness	N/m
λ	Wavelength	m
V_{pH}	Horizontal compressional wave velocity	m/s
V_{pV}	Vertical compressional wave velocity	m/s
V_{sHH}	Horizontal shear wave velocity	m/s
V_{sVV}	Vertical shear wave velocity	m/s
$V_{p\Phi}$	Inclined compressional wave velocity	m/s
$\sigma_{\mathrm{v}}^{'}$	Vertical stress under uniaxial strain	Pascal
$\sigma_{1}^{'}$	The magnitude of maximum effective principal stress	Pascal
ψ	Group angle	degree
ϕ	Phase angle	degree
θ	The angle of maximum effective principal stress; the tilted angle of anisotropy	degree
V_{group}	Group velocity	m/s
V_{phase}	Phase velocity	m/s
a_{ij}	Power lay fitting coefficient for C_{ij}: the constant	dimensionless
b_{ij}	Power lay fitting coefficient for C_{ij}: the multiplier	dimensionless
c_{ij}	Power lay fitting coefficient for C_{ij}: the power	dimensionless
a_{i}	RBF-FD weight for the i^{th} node	dimensionless
U_{H}	Horizontal particle displacement in acoustic TI media	dimensionless

U_{V}	Vertical particle displacement in acoustic TI media	dimensionless
ε	Compressional anisotropy	dimensionless
δ	Shear anisotropy	dimensionless
η	Short offset anisotropy	dimensionless

References

Adams, A. L., Germaine, J. T., Flemings, P. B., and Day-Stirrat, R. J., 2013, Stress induced permeability anisotropy of resedimented Boston Blue Clay: Water Resources Research, **49**(10), 6561–6571.

Abdulhadi, N. O., 2009, An experimental investigation into the stress-dependent mechanical behavior of cohesive soil with application to wellbore instability: Ph.D. dissertation, Massachusetts Institute of Technology.

Arthur, J. R. F., Chua. K. S., Dunstan, T., 1977, Induced anisotropy in a sand: Géotechnique **27**(1):13–30.

Asaka, M., Sekine, T., and Furuya, K., 2016, Geologic cause of seismic anisotropy: A case study from offshore Western Australia: The Leading Edge, **35**(8), 650–728.

Bandyopadhyay, K., 2009, Seismic anisotropy: geological causes and its implications to reservoir geophysics: Ph.D. dissertation, Stanford University.

Bayona, V., Flyer, N., Fornberg, B., and Barnett, G. A., 2017, On the role of polynomials in RBF-FD approximations: II. Numerical solution of elliptic PDEs: Journal of Computational Physics, **332**, 257–273.

Berljavac, J., Mishra, P. K., Slak, J., and Kosec, G., 2020, RBF-FD analysis of 2D time-domain acoustic wave propagation in heterogeneous Earth's subsurface: Preprint, https://arxiv.org/abs/2001.01597.

Collet, O., Gurevich, B., Madadi, M., and Pervukhina, M., 2012, Stress-induced anisotropy model for triaxially stressed rocks: SEG Technical Program Expanded Abstracts 2012, Society of Exploration Geophysicists, 4609–4616.

Crampin, S., Chesnokov, E. M., and Hipkin, R. G., 1984, Seismic anisotropy — the state of the art: II: Geophysical Journal International, **76**(1), 1–16.

Datta D., and Sen M. K., 2016, Estimating a starting model for full-waveform inversion using a global optimization method: Geophysics, **81**(4), R211-R223.

Datta D., Sen M. K., Liu F., and Morton S., 2019, Full-waveform inversion of salt models using shape optimization and simulated annealing: Geophysics, **84**(5), R793-R804.

David, E. C., Brantut, N., Hansen, L. N., and Mitchell, T. M. 2018, Absence of Stress-Induced Anisotropy During Brittle Deformation in Antigorite Serpentinite: Journal of Geophysical Research: Solid Earth, **123**(12), 10,616–10,644.

Dellinger, J., and Vernik, L., 1994, Do traveltimes in pulse-transmission experiments yield anisotropic group or phase velocities?: 59(11), 1774–1779.

Duveneck, E., Milcik, P., Bakker, P. M., and Perkins, C., 2008, Acoustic VTI wave equations and their application for anisotropic reverse-time migration: SEG Technical Program Expanded Abstracts 2012, Society of Exploration Geophysicists, 2186–2190.

Fang, X., Fehler, M. C., and Cheng, A., 2013, Simulation of the effect of stress-induced anisotropy on borehole compressional wave propagation, Geophysics, **79**(4), D205–D216.

Fang, X., Fehler, M., Zhu, Z., Chen, T., Brown, S., Cheng, A., and Nafi Toksöz, M., 2012, Predicting stress-induced anisotropy around a borehole: SEG Technical Program Expanded Abstracts 2012, Society of Exploration Geophysicists, 449–453.

Ferreira, C. 2008, The use of seismic wave velocities in the measurement of stiffness of a residual soil: Ph.D. Thesis, University of Porto.

Fichtner, A., Kennett, B. L. N., and Trampert, J., 2013, Separating intrinsic and apparent anisotropy: Physics of the Earth and Planetary Interiors, **219**, 11–20.

Fornberg, B., and Flyer, N., 2015a, Fast generation of 2-D node distributions for mesh-free PDE discretizations: Computers and Mathematics with Applications, **69**(7), 531–544.

Gurevich, B., and Pervukhina, M., 2010, An analytical model for stress-induced anisotropy of a cracked solid: SEG Technical Program Expanded Abstracts 2010, Society of Exploration Geophysicists, 2517–2521.

Helbig, K., 1994, Foundations of Anisotropy for Exploration Seismics: Pergamon press.

Mahdi Heidari, Maria A. N., and Peter B. F., 2017, Coupling geomechanical modeling with seismic pressure prediction: Geophysics, **83**(5), B253–B267.

Martin, B., Fornberg, B., and St-Cyr, A., 2015, Seismic modeling with radial-basis-function-generated finite differences: Geophysics, **80**(4), T137–T146.

McBride, B. C., Paul, W., and Mark G. R., 1998, The effect of allochthonous salt on the petroleum systems of northern Green Canyon and Ewing Bank (offshore Louisiana), northern Gulf of Mexico: AAPG Bulletin, **82**(5), 1083–1112.

Johnson, J. H., Savage, M. K., and Townend, J., 2011, Distinguishing between stress-induced and structural anisotropy at Mount Ruapehu volcano, New Zealand: Journal of Geophysical Research: Solid Earth, **116**(B12), 1–18.

Kristek, J., Moczo, P., Chaljub, E., and Kristekova, M., 2017, An orthorhombic representation of a heterogeneous medium for the finite-difference modelling of seismic wave propagation: Geophysical Journal International, **208**(2), 1250–1264.

Kuhn, M. R., Sun, W. C., and Wang, Q., 2015, Stress-induced anisotropy in granular materials: fabric, stiffness, and permeability: Acta Geotechnica, **10**(4), 399–419.

Kumar, D., Sen, M. K., and Ferguson, R. J., 2004, Traveltime calculation and prestack depth migration in tilted transversely isotropic media: Geophysics, **69**(1), 37–44.

Lane, C., 2014. The Development of a 2D Ultrasonic Array Inspection for Single Crystal Turbine Blades: Springer press.

Larsson, E., Lehto, E., Heryodono, A., and Fornberg, B., 2013, Stable calculation of differentiation matrices and scattered node stencils based on Gaussian radial basis functions: SIAM Journal on Scientific Computing, **35**(4), A2096–A2119.

Li, B., Liu, Y., Zhao, Y., & Liu, X., 2017, Hybrid absorbing boundary condition for piecewise smooth curved boundary in 2D acoustic finite difference modelling. Exploration Geophysics, **49**(4), 469–483.

Li, W., Schmitt, D. R., Tibbo, M., and Zou, C., 2019, A program to calculate the state of stress in the vicinity of an inclined borehole through an anisotropic rock formation: Geophysics, **84**(5), F103–F118.

Li, X. Y., and Zhang, Y. G., 2011, Seismic reservoir characterization: How can multicomponent data. Journal of Geophysics and Engineering, **8**(2), 123–141.

Luo, G., Nikolinakou, M. A., Flemings P. B., and Hudec M. R., 2012, Geomechanical modeling of stresses adjacent to salt bodies: Part 1—Uncoupled models: AAPG Bulletin, **96**(1), 43–64.

Mah, M., and Schmitt, D. R., 2003, Determination of the complete elastic stiffnesses from ultrasonic phase velocity measurements: Journal of Geophysical Research: Solid Earth, **108**(B1), ECV 6-1– ECV 6-1.

Mavko, G., Mukerji, T., and Godfrey, N., 1995, Predicting stress-induced velocity anisotropy in rocks: Geophysics, **60**(4), 939–1278.

Maultzsch, S., Chapman, M., Liu E., and Li, X., 2003, Modelling frequency-dependent seismic anisotropy in fluid-saturated rock with aligned fractures: implication of fracture size estimation from anisotropic measurements: Geophysical prospecting, **51**(5), 381–392.

Moczo, P., Gregor, D., Kristek, J., and Puente, J., 2019, A discrete representation of material heterogeneity for the finite-difference modelling of seismic wave propagation in a poroelastic medium: Geophysical Journal International, **216**(2), 1072–1099.

Mishra, P. K., Fasshauer, G. E., Sen, M. K., and Ling, L., 2019, A stabilized radial basis-finite difference (RBF-FD) method with hybrid kernels: Computers and Mathematics with Applications, **77**(9), 2354–2368.

Nikolinakou, M. A., Hedari, M., Flemings P. B., and Hudec M. R., 2018, Geomechanical modeling of pore pressure in evolving salt systems: Marine and Petroleum Geology, **93**, 272–286.

Nikolinakou, M. A., Luo, G., Hudec, M. R., and Flemings P. B., 2012, Geomechanical modeling of stresses adjacent to salt bodies: Part 2—Poroelastoplasticity and coupled overpressures: AAPG Bulletin, **96**(1), 65–85.

Rasolofosaon, P., 1998, Stress-induced seismic anisotropy revisited: Revue de l'Institut Français du petrol, **53**(5), 679–692.

Oda, M., Nemat-Nasser, S., and Konishi, J., 1985, Stress-induced anisotropy in granular masses: Soils Found, **25**(3), 85–97.

Ong, O. N., Schmitt, D. R., Kofman, R. S., and Haug, K., 2016, Static and dynamic pressure sensitivity anisotropy of a calcareous shale: Geophysical Prospecting, **64**(4), 875–897.

Ouadfel, H., and Rothenburg, L., 1999, An algorithm for detecting inter-ellipsoid contacts: Computers and Geotechnics, **24**(4), 245–263.

Ouadfel, H., and Rothenburg, L., 2001, Stress–force–fabric relationship for assemblies of ellipsoids: Mechanics of Materials, **33**(4), 201–221.

Ranjpour, D., 2020, Stiffness and anisotropy characterization of cechanically-compressed cohesive soils using directional wave propagation: Ph.D. Thesis, Tufts University.

Passelègue, F. X., Pimienta, L., Faulkner, D., Schubnel, A., Fortin, J., and Guéguen, Y., 2018, Development and Recovery of Stress-Induced Elastic Anisotropy During Cyclic Loading Experiment on Westerly Granite: Geophysical Research Letters, **45**(16), 8156–8166.

Prioul, R., Bakulin, A., and Bakulin, V., 2004, Nonlinear rock physics model for estimation of 3D subsurface stress in anisotropic formations: Theory and laboratory verification: Geophysics, **69**(2), 318–628.

Ren, Z., and Li, Z., 2019, High-order temporal and implicit spatial staggered-grid finite-difference operators for modelling seismic wave propagation: Geophysical Journal International, **217**(2), 844–865.

Sarkar, D., Bakulin, A., and Kranz, B., 2003, Anisotropic inversion of seismic data for stressed media: Theory and a physical- modeling study on berea sandstone: Geophysicis, 1–15.

Sarout, J., Delle Piane, C., Nadri, D., Esteban, L., and Dewhurst, D. N., 2015, A robust experimental determination of Thomsen's δ parameter: Geophysics, **80**(1), A19–A24.

Sayers, C. M., and Dasgupta, S., 2019, A predictive anisotropic rock-physics model for estimating elastic rock properties of unconventional shale reservoirs: The Leading Edge, **38**(5), 358–365.

Schoenberg, M., and Muir, F., 1989, A calculus for finely layered anisotropic media: Geophysics, **54**(5), 581–589.

Schoenberg, M., and Sayers C. M., 1995, Seismic anisotropy of fractured rock: Geophysics, **60**(1), 204–211.

Sen, M. K., and Stoffa P. L., 1995, Global Optimization Methods in Geophysical Inversion: Elsevier Science.

Shelley, A., Savage, M., Williams, C., Aoki, Y., and Gurevich, B., 2014, Modeling shear wave splitting due to stress-induced anisotropy, with an application to Mount Asama Volcano, Japan: Journal of Geophysical Research: Solid Earth, **119**(5), 4269–4286.

Spikes, K. T. ,2014, Error estimates of elastic components in stress-dependent VTI media: Journal of Applied Geophysics, **108**, 110–123.

Thomsen, L., 1986, Weak elastic anisotropy: Geophysics, **51**(10), 1954–1966.

Tromp, J., and Trampert, J., 2018, Effects of induced stress on seismic forward modelling and inversion: Geophysical Journal International, **213**(2), 851–867.

Tromp, J., Marcondes, M. L., Wentzcovitch, R. M. M., and Trampert, J., 2019, Effects of Induced Stress on Seismic Waves: Validation Based on Ab Initio Calculations: Journal of Geophysical Research: Solid Earth, **124**(1), 729–741.

Tsvankin, I., 2001, Seismic Signatures and Analysis of Reflection Data in Anisotropic Media: Pergamon press.

Verdon, J. P., Angus, D., Kendall, J. M., and Hall, S. A., 2008, The effect of microstructure and nonlinear stress on anisotropic seismic velocities: Geophysics, **73**(4), D41–D51.

Vestrum, R. 1994, Group and Phase-Velocity Inversions for the General Anisotropic Stiffness Tensor: Master Thesis, University of Calgary.

Wang, N., Montagner, J., Burgos, G., Capdeville, Y., and Yu, D., 2015, Intrinsic versus extrinsic seismic anisotropy: Surface wave phase velocity inversion: Comptes Rendus Geoscience, **347**(2), 66–76.

Wang, N., Montagner, J. P., Fichtner, A., and Capdeville, Y., 2013, Intrinsic versus extrinsic seismic anisotropy: The radial anisotropy in reference Earth models: Geophysical Research Letters, **40**(16), 4284–4288.

Werner, U., and Shapiro, S. A., 1998, Intrinsic anisotropy and thin multilayering - Two anisotropy effects combined: Geophysical Journal International, **132**(2), 363–373.

Xu, S., and Liu, Y., 2016, Acoustic TTI Modelling with a Time-space Domain Finite-difference Stencil: 78th EAGE Conference & Exhibition, 1–5.

Yan, F., Han, D., and Yao, Q., 2016, Physical constraints on c 13 and δ for transversely isotropic hydrocarbon source rocks. Geophysical Prospecting, **64**(6), 1524–1536.

Zhang, J., Zhang, G., and Huang, L. H., 2019, Crack fluid identification of shale reservoir based on stress-dependent anisotropy: Applied Geophysics, **16**, 209–217.

Zheng, Y., Tang, X., and Patterson, D. J., 2009, Identifying stress-induced anisotropy and stress direction using cross-dipole acoustic logging: SPWLA 50th Annual Logging Symposium, Society of Petrophysicists and Well-Log Analysts.

Vita

Xin Liu was born in a village in Shifang, China during the fall of 1993. Xin had been lived there for 18 years before he went to Beijing and obtained his Bachelor and Master degrees in Geophysics. Xin Liu continued his education upon receiving an offer to conduct research while earning his Master of Science in Geological Sciences with emphasis in Geophysics at the University of Texas at Austin – Jackson School of Geosciences. Xin graduated in the winter of 2021, where he went back to China for a new job.

Email: lx2wqy@utexas.edu

This thesis was written by Xin Liu.